



# An empirical model of high-latitude ionospheric conductances based on EISCAT observations

Liisa Juusola<sup>1,2</sup>, Ilkka Virtanen<sup>3</sup>, Spencer Mark Hatch<sup>4</sup>, Heikki Vanhamäki<sup>3</sup>, Maxime Grandin<sup>2</sup>, Noora Partamies<sup>5</sup>, Urs Ganse<sup>1</sup>, Ilja Honkonen<sup>2</sup>, Abiyot Workayehu<sup>1</sup>, Antti Kero<sup>6</sup>, and Minna Palmroth<sup>1,2</sup>

<sup>1</sup>Department of Physics, University of Helsinki, Helsinki, Finland

<sup>2</sup>Finnish Meteorological Institute, Helsinki, Finland

<sup>3</sup>Space Physics and Astronomy Unit, University of Oulu, Oulu, Finland

<sup>4</sup>Department of Physics and Technology, University of Bergen, Bergen, Norway

<sup>5</sup>Department of Arctic Geophysics, University Centre in Svalbard (UNIS), Longyearbyen, Norway

<sup>6</sup>Sodankylä Geophysical Observatory, University of Oulu, Sodankylä, Finland

**Correspondence:** Liisa Juusola (liisa.juusola@fmi.fi)

**Abstract.** Conductances are key properties of the ionospheric electrodynamics and the difficulty of measuring them directly is a significant limitation to the usefulness of many analysis techniques. We have utilized all available field-aligned observations from the EISCAT incoherent scatter ultra-high frequency (UHF) radar since 2001 and from the 42 m EISCAT Svalbard Radar (ESR) since 1998 to develop a new empirical model for estimating the high-latitude ionospheric Hall and Pedersen conductances. The solar radiation component of the model is parametrized with the solar zenith angle and the  $F_{10.7}$  index, and the auroral precipitation component is parametrized with the magnetic local time and the divergence-free part of the horizontal ionospheric current density, which is obtained from ground-based magnetic field observations. We have also derived a new technique based on spherical elementary current systems that can be used to solve for the ionospheric potential electric field and field-aligned current density from known ionospheric conductances and ground-based magnetic field observations, taking into account induction in the ionosphere and in the ground. The new empirical conductance model and solver were applied to IMAGE magnetometer network observations. Comparison of the results with Swarm satellite observations showed reasonable agreement in the electric field profile and direction of the field-aligned current, but in the post-midnight sector the amplitudes tended to be weaker than those observed by Swarm. The combination of the new conductance model and analysis technique allows estimating the key properties of ionospheric electrodynamics from ground-based magnetic field observations.

## 1 Introduction

Key properties of the ionospheric electrodynamics are electric fields, currents, and height-integrated conductivities, also called conductances. They are tightly coupled to adjacent domains: Field-aligned currents and the potential electric field connect the ionosphere and the magnetosphere, providing a window to processes in the vast and distant near-Earth space through observations of the more compact and conveniently located ionosphere. Joule heating due to the currents affects thermospheric density, with poorly understood but occasionally disastrous effects on satellite orbits (e.g., Zhang et al., 2022). The inductive



electric field interacts with the conducting ground (e.g., Juusola et al., 2024), driving potentially hazardous geomagnetically induced currents (GICs) in technological conductor networks.

A crucial limitation to studying ionospheric electrodynamics is the scarcity of simultaneous observations of the key properties of ionospheric electrodynamics in the same region. Long time series of observations at a comparable and sufficiently detailed spatial and temporal resolution would be ideal, in order to cover all relevant event types. Global or even regional observations of the ionospheric conductance distribution are especially difficult to obtain (see, e.g., Robinson et al., 2020; Palmroth et al., 2021; Wang and Zou, 2022). However, at large spatial scales ( $\sim 1000$  km) and 10 min time resolution, Green et al. (2007) suggest that they could be estimated by combining the ionospheric currents from SuperMAG (Gjerloev, 2012) and Active Magnetosphere and Planetary Electrodynamics Response Experiment (AMPERE; Anderson et al., 2002) observations and the electric field from Super Dual Auroral Radar Network (SuperDARN; Chisham et al., 2007) observations.

The International Monitor for Auroral Geomagnetic Effects (IMAGE) magnetometer network, located in Fennoscandia and surrounding areas, provides a continuous time series of meso-scale ( $\sim 100$  km), 10 s ground-based magnetic field observations that cover several solar cycles. From these data, it is possible to derive the divergence-free (DF) part of the horizontal current density  $\mathbf{J}_{DF}$  and the DF (i.e., inductive) part of the horizontal ionospheric electric field  $\mathbf{E}_{DF}$  due to telluric and DF ionospheric currents (Pirjola and Viljanen, 1998; Madelaire et al., 2024; Juusola et al., 2024). Above the ionospheric horizontal current sheet, the curl-free (CF) horizontal ionospheric currents and field-aligned currents also contribute to the DF electric field, although Vanhamäki et al. (2007) argue that this DF electric field should be very small.

There are no regional potential electric field data available in the IMAGE area. However, if ionospheric conductances were available, the CF part of the horizontal electric field  $\mathbf{E}_{CF}$  (i.e., potential electric field) and the CF part of the horizontal current density  $\mathbf{J}_{CF}$  could be calculated using the expressions from Juusola et al. (2024),

$$\mathbf{E} = \mathbf{E}_{CF} + \mathbf{E}_{DF} \quad (1)$$

$$\mathbf{J} = \mathbf{J}_{CF} + \mathbf{J}_{DF} \quad (2)$$

$$\mathbf{J} = \Sigma_P \mathbf{E} + \Sigma_H \mathbf{E} \times \hat{\mathbf{e}}_r \quad (3)$$

$$(\nabla \times \mathbf{J})_r = [\nabla \Sigma_P \times (\mathbf{E}_{CF} + \mathbf{E}_{DF})]_r + \Sigma_P [\nabla \times \mathbf{E}_{DF}]_r + [\nabla \Sigma_H \times ((\mathbf{E}_{CF} + \mathbf{E}_{DF}) \times \hat{\mathbf{e}}_r)]_r - \Sigma_H (\nabla \cdot \mathbf{E}_{CF}) \quad (4)$$

$$\nabla \cdot \mathbf{J} = \nabla \Sigma_P \cdot (\mathbf{E}_{CF} + \mathbf{E}_{DF}) + \Sigma_P \nabla \cdot \mathbf{E}_{CF} + \nabla \Sigma_H \cdot [(\mathbf{E}_{CF} + \mathbf{E}_{DF}) \times \hat{\mathbf{e}}_r] + \Sigma_H (\nabla \times \mathbf{E}_{DF})_r. \quad (5)$$

Here,  $\mathbf{J}$  is the ionospheric sheet current density perpendicular to the main magnetic field,  $\mathbf{E}$  is the electric field perpendicular to the magnetic field,  $\Sigma_P$  is the Pedersen conductance perpendicular to the magnetic field and parallel to the electric field,  $\Sigma_H$  is the Hall conductance perpendicular to both the magnetic and electric field, and  $\hat{\mathbf{e}}_r$  is a unit vector in the direction of the assumed radial magnetic field lines. This approach has a similar basis as the KRM technique (Kamide et al., 1981), the Assimilative Mapping of Ionospheric Electrodynamics (AMIE; Richmond and Kamide, 1988; Richmond, 1992), and Local Mapping of Polar Ionospheric Electrodynamics (Lompe; Laundal et al., 2022a), but unlike those models, it takes  $\mathbf{E}_{DF}$  into account as well. In some dynamical situations, inductive effects are not negligible and the ionospheric electric field is not a pure CF field, but can have a significant DF part (Vanhamäki et al., 2007; Madelaire et al., 2024).



There are two main sources of  $\Sigma_P$  and  $\Sigma_H$ : photoionization, which is caused by solar radiation on the dayside, and im-  
55 pact ionization, which is caused by auroral precipitation. Moen and Brekke (1993) have derived an empirical model for the  
solar radiation component as a function of the solar zenith angle  $\chi$  and  $F_{10.7}$  solar flux based on nine days of data from the  
European Incoherent Scatter Scientific Association (EISCAT) incoherent scatter radar. Another model with slightly different  
parametrization was developed by Ieda et al. (2015). Ahn et al. (1998), on the other hand, have derived an empirical model for  
the precipitation components of  $\Sigma_P$  and  $\Sigma_H$  as a function of horizontal and vertical ground magnetic field perturbations and  
60 magnetic local time (MLT) based on auroral-zone Chatanika incoherent scatter radar data. This model has been incorporated  
into AMIE.

We will utilize a newly processed data set of  $\Sigma_P$  and  $\Sigma_H$ , derived from all available field-aligned EISCAT Ultra High  
Frequency (UHF) radar observations between January 2001 and January 2024 and from the 42 m EISCAT Svalbard Radar  
(ESR) between October 1998 and January 2024, to continue the work of Moen and Brekke (1993) and Ahn et al. (1998). The  
65 UHF radar is located in Tromsø in Northern Norway and the ESR radar near Longyearbyen in Svalbard. Our aim is to develop  
an empirical model for  $\Sigma_P$  and  $\Sigma_H$  that would make it possible to estimate  $E_{CF}$  and  $J_{CF}$  from  $J_{DF}$  and  $E_{DF}$ . Instead of  
ground magnetic field variations, which are often contaminated by signatures from induced telluric currents (Juusola et al.,  
2020), we will use the ionospheric  $J_{DF}$  to parametrize the precipitation-dependent component. Furthermore, we will show  
that the empirical model of Moen and Brekke (1993), which is based on nine days of EISCAT data, is not ideal for describing  
70 the newly processed, long time series of EISCAT conductances, and derive a new, modified version by simultaneously fitting  
both the solar radiation and precipitation component models to the observations.

An empirical model that predicts the precipitation component of  $\Sigma_P$  and  $\Sigma_H$  based on  $J_{DF}$  has the advantage that the con-  
ductances have the same spatial resolution as  $J_{DF}$ , and they follow the dynamics of  $J_{DF}$ , unlike for example climatological  
models that use some other parameter as input (e.g., Newell et al., 2009; Machol et al., 2012; Hatch et al., 2024). Further-  
75 more, the time series is not truncated due to dependency on data from another instrument. In the near future, EISCAT\_3D will  
start operations in northern Fennoscandia and provide detailed, volumetric observations of the ionospheric conductivities and  
electric fields. Our model can provide meso-scale context to the regionally more limited EISCAT3D observations.

The structure of the study is as follows: the data and methods are described in Section 2, the empirical model is developed  
and validated in Section 3, and its performance is discussed in Section 4. The conclusions are summarised in Section 5.

## 80 2 Data and methods

### 2.1 EISCAT radar data

#### 2.1.1 Data selection

All data available from the EISCAT UHF radar in Tromsø from January 2001 to January 2024 and from the 42 m ESR near  
Longyearbyen from October 1998 to January 2024 were downloaded from the Madrigal data base (Madrigal, 2025). UHF data  
85 measured before a major system upgrade in 2000 were not used, because the amount of data in Madrigal is very small and



the radar modes and data analysis were different from those used after the upgrade. Data less than one year old in January 2025 were not used due to the embargo rules of EISCAT. The EISCAT data in Madrigal are plasma parameters fitted to measured incoherent scatter spectra using the Grand Unified Incoherent Scatter Design and Analysis Program (GUISDAP; Lehtinen and Huuskonen, 1996; Häggström, 2025). The fitted parameters are electron density ( $N_e$ ), electron temperature, ion temperature, and line-of-sight bulk plasma velocity. In this study, we use electron densities, and select only electron density profiles measured with a magnetic field aligned radar beam and with 30 to 120 s time resolution. The profiles were cleaned by removing individual data points according to the following conditions: the GUISDAP fit must be flagged as successful, relative error in  $N_e$  must be smaller than 0.5, chi-square of the fit must be smaller than 10, ion temperature must be larger than 50 K, and  $N_e < 10^{12} \text{ m}^{-3}$  below 95 km altitude. The last two conditions remove clearly erroneous results that are not captured automatically by GUISDAP. Logarithm of  $N_e$  was then linearly interpolated to 1 km range resolution between 75 and 330 km altitudes to create a consistent data set. Finally, profiles that contain electron densities larger than  $5 \cdot 10^{12} \text{ m}^{-3}$  after the interpolation were rejected to remove strong, non-ionospheric echoes, e.g., from satellites.

### 2.1.2 Conductivity calculation

Hall and Pedersen conductivities  $\sigma_H$  and  $\sigma_P$  were calculated from the interpolated  $N_e$  as

$$\sigma_P = \left( \frac{1}{m_e \nu_{en}} \frac{\nu_{en}^2}{\nu_{en}^2 + \omega_{ce}^2} + \frac{1}{m_i \nu_{in}} \frac{\nu_{in}^2}{\nu_{in}^2 + \omega_{ci}^2} \right) N_e e^2 \quad (6)$$

$$\sigma_H = \left( \frac{1}{m_e \nu_{en}} \frac{\omega_{ce} \nu_{en}}{\nu_{en}^2 + \omega_{ce}^2} - \frac{1}{m_i \nu_{in}} \frac{\omega_{ci} \nu_{in}}{\nu_{in}^2 + \omega_{ci}^2} \right) N_e e^2, \quad (7)$$

where  $m_e$  and  $m_i$  are the electron and ion mass,  $e$  is the unit charge,  $\omega_{ce}$  and  $\omega_{ci}$  are the cyclotron or gyrofrequency of electrons and ions, and  $\nu_{en}$  and  $\nu_{in}$  are the electron-neutral and ion-neutral collision frequencies (Schunk and Nagy, 2009).

First, neutral atmospheric parameters were obtained using the NRLMSISE-00 model (Picone et al., 2002) for the location and time of each measurement. Ion-neutral collision frequencies for molecular ions (75% NO+ and 25% O2+), atomic ions (O+), and electron-neutral collision frequencies were calculated using formulas of Schunk and Nagy (2009). The NRLMSISE-00 neutral temperature ( $T_n$ ) was used for ion ( $T_i$ ) and electron ( $T_e$ ) temperatures ( $T_i = T_e = T_n$ ), because the fitted  $T_i$  and  $T_e$  are often very noisy, especially when  $N_e$  is low.  $T_e$  and  $T_i$  may be increased above  $T_n$  by particle precipitation and Joule heating, respectively. Although the ion-neutral collisions frequencies of Schunk and Nagy (2009) are temperature dependent, Baloukidis et al. (2023) reported that doubling the model  $T_n$  has only a very small effect on the Pedersen conductance estimates. We have made a similar test for both Pedersen and Hall conductances, and found that doubling  $T_e$ ,  $T_i$ , or both has only very small effect on both Pedersen and Hall conductances.

Magnetic field intensities were calculated with the International Geomagnetic Reference Field (IGRF-13) model (Alken et al., 2021), and these were used to calculate gyrofrequencies. Pedersen and Hall conductivities were calculated using the modelled collision frequencies and gyrofrequencies, the measured  $N_e$ , and molecular-to-atomic ion density ratio from the International Reference Ionosphere (IRI) model (Bilitza et al., 2022). Standard deviations (STD) of the conductivities were calculated using STD of  $N_e$  from the GUISDAP fits, which is expected to be the dominant source of error. The model values



of collision frequencies and gyrofrequencies, which are based on well-established models of the geomagnetic field and the neutral atmosphere, were considered exact.

### 120 2.1.3 Height integration and final cleaning

Hall and Pedersen conductances were height-integrated from the conductivities, except if the profile contained extremely small ( $N_e < 10^{q_1-0.2}$ , where  $q_1$  is the 0.001 quantile of the  $\log_{10}(N_e)$  values) or large ( $N_e > 10^{q_2+0.2}$ , where  $q_2$  is the 0.999 quantile of the  $\log_{10}(N_e)$  values)  $N_e$ . This was done in order to remove strong satellite echoes. All data were plotted, and radar experiments that suffered from obvious technical problems or did not have sufficient altitude coverage for the conductance calculation were manually removed. Duplicate analysis runs of the same data were also removed.

125 Remaining satellite echoes and noise spikes (or minima) caused by technical issues were removed as follows: For both Pedersen and Hall conductances, the standard deviation and mean of data points within 10 points from point  $i$  in the time series, excluding point  $i$ , were calculated. Point  $i$  was flagged as a noise spike, if either of the conductances at point  $i$  deviated more than 10 standard deviations from the corresponding mean values. All rejected points were removed from the final data vectors.

130 Pedersen and Hall conductivity data points where the  $N_e$  profiles did not reach low enough altitudes were rejected if the following conditions were satisfied: 1) Conductivity at the lowest measured altitude was more than  $2 \cdot 10^{-4}$  S/m or more than half of the maximum conductivity. 2) The conductivity maximum was located less than 5 km above the lowest measured altitude. In the end, we were left with 609 776  $\Sigma_P$  values and 605 774  $\Sigma_H$  values from UHF and 925 900  $\Sigma_P$  values and 923 638  $\Sigma_H$  values from ESR. Their magnetic local time distributions are illustrated in Figures 3e and 4e. These figures will be discussed in more detail in section 3.1.

## 2.2 IMAGE magnetometer network data

We have used 10 s ground magnetic field measurements from the IMAGE magnetometers (Juusola et al., 2025). For data before 2015, we have used the method by van de Kamp (2013) to subtract the long-term baseline (including instrument drifts, etc.), any jumps in the data, and the diurnal variation from the variometer data. For 2015 onwards, we have first corrected the data for any jumps and spikes and then subtracted a ten-day sliding median. The ten-day sliding median was calculated for the midnight of each day and the baseline values in between were interpolated using a cosine curve.

145 The remaining variation magnetic field consists of an external part mainly due to ionospheric electric currents but with some magnetospheric contribution as well, and an internal part due to induced telluric currents in the conducting ground. We have used the two-dimensional (2-D) Spherical Elementary Current System (SECS) method (Amm, 1997; Amm and Viljanen, 1999; Pulkkinen et al., 2003a, b; McLay and Beggan, 2010; Weygand et al., 2011; Juusola et al., 2016b; Marsal et al., 2017, 2020; Juusola et al., 2020; Laundal et al., 2021; Vanhamäki and Juusola, 2020; Walker et al., 2023; Juusola et al., 2023a, b, 2024) to estimate the ionospheric  $J_{DF}$  for the time integration intervals of EISCAT  $\Sigma_P$  and  $\Sigma_H$  at the locations of the field-aligned measurements, (69.583°, 19.210°) geodetic latitude and longitude for UHF and (78.09°, 16.02°) for ESR. For each value of  $\Sigma_P$



150 and  $\Sigma_H$ , the corresponding value of  $\mathbf{J}_{DF}$  was obtained as a mean of the  $\mathbf{J}_{DF}$  values during the radar measurement integration time.

### 2.3 Ionospheric electrodynamics with the 2-D SECS method

The divergence-free part of the ionospheric horizontal current density can be expressed in terms of 2D DF SECS functions. The current density of the divergence-free (DF) 2D SECS is

$$155 \quad \mathbf{J}_{DF}(t, \theta') = \frac{I_{DF}(t)}{4\pi R} \hat{\mathbf{e}}_{\phi'} \begin{cases} \tan\left(\frac{\theta'}{2}\right) \cot^2\left(\frac{\theta_0}{2}\right), & \theta' < \theta_0 \\ \cot\left(\frac{\theta'}{2}\right), & \theta' \geq \theta_0 \end{cases} \quad (8)$$

where  $R$  is the radius of the ionosphere,  $\theta'$  is the colatitude in the SECS coordinates,  $\hat{\mathbf{e}}_{\phi'}$  is a unit vector in the zonal direction in the SECS coordinates, and  $I_{DF}(t)$  is the time-dependent DF SECS amplitude. The curl of  $\mathbf{J}_{DF}$  is uniformly distributed over a spherical cap defined by the colatitude  $\theta_0$

$$(\nabla \times \mathbf{J}_{DF})_r = -\frac{I_{DF}(t)}{4\pi R^2} + \begin{cases} \frac{I_{DF}(t)}{A}, & \theta' < \theta_0 \\ 0, & \theta' \geq \theta_0 \end{cases} \quad (9)$$

160 where  $A$  is the area of the spherical cap,

$$A = 2\pi R^2(1 - \cos\theta_0) \quad (10)$$

and can be set to equal the SECS grid cell area. The magnetic field associated with  $\mathbf{J}_{DF}$  is

$$\mathbf{B} = \mathbf{B}_r + \mathbf{B}_{\theta'} \quad (11)$$

$$165 \quad B_r(t, r, \theta') = \frac{I_{DF}(t)\mu_0}{4\pi} \frac{1}{r} \left( \frac{R}{\sqrt{r^2 - 2rR\cos\theta' + R^2}} + \begin{cases} -1, & r < R \\ -R/r, & r \geq R \end{cases} \right) \quad (12)$$

$$B_{\theta'}(t, r, \theta') = -\frac{I_{DF}(t)\mu_0}{4\pi} \frac{1}{r \sin\theta'} \left( \frac{r - R\cos\theta'}{\sqrt{r^2 - 2rR\cos\theta' + R^2}} + \begin{cases} \cos\theta', & r < R \\ -1, & r > R \end{cases} \right) \quad (13)$$

where  $\mu_0$  is the vacuum permeability. There is a small inconsistency between the magnetic field of Eq. 12–13 and the current density of Eq. 8, because the magnetic field expressions have been derived for  $\theta_0 = 0$ . However, as discussed by Vanhamäki and Juusola (2020), this does not appear to affect practical applications.

The DF SECS poles are placed on uniform or nonuniform grids in the region of interest. With IMAGE we typically use grids with  $0.5^\circ$  latitude and  $1^\circ$  longitude resolution at 1 m depth and at 90 km altitude. The amplitudes  $I_{DF}$  are determined



by fitting the superposed magnetic field of the SECSs to the three components of the measured magnetic field. The inductive electric field associated with temporal changes in the  $\mathbf{J}_{DF}$  amplitude is given by Faraday's law

$$175 \quad (\nabla \times \mathbf{E}_{DF})_r = -\frac{\partial B_r}{\partial t} \quad (14)$$

as

$$\mathbf{E}_{DF}(t, r, \theta') = -\frac{\partial I_{DF}(t)}{\partial t} \frac{\mu_0}{4\pi} \hat{\mathbf{e}}_{\phi'} \frac{1}{r \sin \theta'} \left( \sqrt{r^2 - 2rR \cos \theta' + R^2} + \begin{cases} r \cos \theta' - R, & r < R \\ R \cos \theta' - r, & r \geq R \end{cases} \right) \quad (15)$$

(Juusola et al., 2024). The time derivative of the SECS amplitudes can be estimated as

$$\frac{\partial I_{DF}}{\partial t} \approx \frac{I_{DF}(t) - I_{DF}(t - \Delta t)}{\Delta t}, \quad (16)$$

180 where  $\Delta t$  is the time step of the data, 10 s for IMAGE.

The curl-free (CF) part of the horizontal ionospheric current density can be expressed in terms of CF 2D SECS functions,

$$\mathbf{J}_{CF}(t, \theta') = \frac{I_{CF}(t)}{4\pi R} \hat{\mathbf{e}}_{\theta'} \begin{cases} \tan\left(\frac{\theta'}{2}\right) \cot^2\left(\frac{\theta_0}{2}\right), & \theta' < \theta_0 \\ \cot\left(\frac{\theta'}{2}\right), & \theta' \geq \theta_0 \end{cases} \quad (17)$$

$$\nabla \cdot \mathbf{J}_{CF} = -j_r = -\frac{I_{CF}(t)}{4\pi R^2} + \begin{cases} \frac{I_{CF}(t)}{A}, & \theta' < \theta_0 \\ 0, & \theta' \geq \theta_0 \end{cases} \quad (18)$$

185 where  $I_{CF}$  is the CF SECS amplitude and  $j_r$  is the radial current density. The magnetic field of  $\mathbf{J}_{CF}$  is

$$\mathbf{B}(t, r, \theta') = -\frac{\mu_0 I_{CF}(t)}{4\pi r} \hat{\mathbf{e}}_{\phi'} \begin{cases} 0, & r < R \\ \tan\left(\frac{\theta'}{2}\right) \cot^2\left(\frac{\theta_0}{2}\right), & r > R, \theta' < \theta_0 \\ \cot\left(\frac{\theta'}{2}\right), & r > R, \theta' \geq \theta_0 \end{cases} \quad (19)$$

Similarly, the CF part of the ionospheric horizontal electric field can be expressed as a superposition of 2D CF SECS functions,

$$\mathbf{E}_{CF}(t, \theta') = \frac{Q_{CF}(t)}{4\pi R} \hat{\mathbf{e}}_{\theta'} \begin{cases} \tan\left(\frac{\theta'}{2}\right) \cot^2\left(\frac{\theta_0}{2}\right), & \theta' < \theta_0 \\ \cot\left(\frac{\theta'}{2}\right), & \theta' \geq \theta_0 \end{cases} \quad (20)$$

$$190 \quad \nabla \cdot \mathbf{E}_{CF} = \frac{\rho}{\epsilon_0} = -\frac{Q_{CF}(t)}{4\pi R^2} + \begin{cases} \frac{Q_{CF}(t)}{A} & \theta' < \theta_0 \\ 0, & \theta' \geq \theta_0 \end{cases} \quad (21)$$



where  $Q_{CF}$  is the CF SECS amplitude,  $\rho$  is the charge density, and  $\epsilon_0$  is the vacuum permittivity. In addition to the CF electric field, it is often useful to determine the associated electric potential  $\Phi_E$ ,

$$\mathbf{E}_{CF}(t, \theta') = -\nabla \Phi_E(t, \theta') = -\frac{1}{R} \frac{\partial \Phi_E(t, \theta')}{\partial \theta'} \hat{\mathbf{e}}_{\theta'} \quad (22)$$

$$\Phi_E(t, \theta') = -R \int_0^{\theta'} E_{CF, \theta}(t, \theta) d\theta = \frac{Q_{CF}(t)}{4\pi} \begin{cases} \cot^2 \frac{\theta_0}{2} \ln \left( \cos^2 \frac{\theta'}{2} \right), & \theta' < \theta_0 \\ \cot^2 \frac{\theta_0}{2} \ln \left( \cos^2 \frac{\theta_0}{2} \right) - \ln \left( \sin^2 \frac{\theta'}{2} \right) + \ln \left( \sin^2 \frac{\theta_0}{2} \right), & \theta' \geq \theta_0 \end{cases} \quad (23)$$

where we have set  $\Phi_E(t, 0) = 0$ .

If  $\mathbf{J}_{DF}$ ,  $\mathbf{E}_{DF}$ , the Pedersen conductance  $\Sigma_P$  and the Hall conductance  $\Sigma_H$  are known,  $\mathbf{E}_{CF}$  and  $\mathbf{J}_{CF}$  can be determined using Eq. 4–5. First, we write Eq. 4 in the form (cf. Juusola et al., 2024)

$$\begin{aligned} \sum_j \left[ [-(\nabla \Sigma_P)_{\phi, i} - (\nabla \Sigma_H)_{\theta, i}] g_{i, j}^{E_{CF, \theta}} + [(\nabla \Sigma_P)_{\theta, i} - (\nabla \Sigma_H)_{\phi, i}] g_{i, j}^{E_{CF, \phi}} + \Sigma_{H, i} \frac{1}{4\pi R^2} \right] Q_{CF, j} - \Sigma_{H, i} \frac{Q_{CF, i}}{A_i} \\ = \frac{I_{DF, i}}{A_i} - \sum_j \frac{I_{DF, j}}{4\pi R^2} - [ [-(\nabla \Sigma_P)_{\phi, i} - (\nabla \Sigma_H)_{\theta, i}] E_{DF, \theta, i, j} + [(\nabla \Sigma_P)_{\theta, i} - (\nabla \Sigma_H)_{\phi, i}] E_{DF, \phi, i, j} + \Sigma_P (\nabla \times \mathbf{E}_{DF})_r ]. \end{aligned} \quad (24)$$

Here, we have denoted the geometry-dependent components of  $\mathbf{E}_{CF}$  (Eq. 20) by  $g$ . We can use this expression to solve for  $Q_{CF, i}$ , at grid points  $i$ . Writing Eq. 5 in the form

$$\begin{aligned} \frac{I_{CF, i}}{A_i} - \sum_j \frac{I_{CF, j}}{4\pi R^2} = \sum_j \left[ [(\nabla \Sigma_P)_{\theta, i} - (\nabla \Sigma_H)_{\phi, i}] E_{DF, \theta, i, j} + [(\nabla \Sigma_P)_{\phi, i} + (\nabla \Sigma_H)_{\theta, i}] E_{DF, \phi, i, j} \right] \\ + \sum_j \left[ [(\nabla \Sigma_P)_{\theta, i} - (\nabla \Sigma_H)_{\phi, i}] g_{i, j}^{E_{CF, \theta}} + [(\nabla \Sigma_P)_{\phi, i} + (\nabla \Sigma_H)_{\theta, i}] g_{i, j}^{E_{CF, \phi}} - \Sigma_{P, i} \frac{1}{4\pi R^2} \right] Q_{CF, j} + \Sigma_{P, i} \frac{Q_{CF, i}}{A_i}, \end{aligned} \quad (25)$$

we can solve for the CF SECS amplitudes  $I_{CF, i}$ . The problem can be made more straightforward with the approximation

$$\frac{I_{CF, i}}{A_i} - \sum_j \frac{I_{CF, j}}{4\pi R^2} \approx \frac{I_{CF, i}}{A_i}. \quad (26)$$

Globally, the sum of all amplitudes is expected to be approximately zero. In local applications, the sum can be non-zero, but as it represents the global sum, more realistic results are in fact obtained by discarding the term.

## 2.4 Swarm data

### 2.4.1 Electric field

We have used the Python package viresclient (Smith et al., 2025) to access Swarm Thermal Ion Imager (TII) cross-track ion flow velocity (“Viy”) measurements, satellite velocity (“VsatC”, “VsatE”, “VsatN”), and geomagnetic field models (“B\_NEC\_CHAOS-Core”, “B\_NEC\_CHAOS-Static”, “B\_NEC\_CHAOS-MMA-Primary”, “B\_NEC\_CHAOS-MMA-Secondary”) from the European Space Agency’s VirES for Swarm service (VirES, 2025). These data are available in the collection “SW\_EXPT\_EFIx\_TCT02”,



215 which is described to contain 2 Hz cross-track ion flows. We have only downloaded data northward of quasi-dipole latitude  $44^\circ$ , which is the low-latitude boundary used for EFI TII cross-track flow calibration, and data that are flagged calibrated, as indicated by the second bit of the quantity `Quality_flags` being set to 1 (Burchill and Knudsen, 2020). The measurements are provided in satellite track coordinates where the unit vector  $\hat{e}_x$  is in the direction of the satellite velocity,  $\hat{e}_z$  points radially downward, and  $\hat{e}_y = -\hat{e}_x \times \hat{e}_z$ . The magnetic field model data are provided in the North-East-Centre (NEC) reference frame.

220 The electric field at Swarm altitude was obtained from the cross-track ion velocity  $V_{i,y}$  as  $E_x = -V_{i,y}B_{model,C}$  and mapped to the altitude of the horizontal current sheet by multiplying by  $\sqrt{B_{IGRF,J_{DF}}/B_{IGRF,sat}}$ , where the IGRF amplitude was obtained using Laundal et al. (2022b). The corresponding component from the IMAGE electric field north ( $E_N$ ) and east ( $E_E$ ) components was obtained as

$$E_x = E_N \frac{V_{sat,N}}{\sqrt{V_{sat,N}^2 + V_{sat,E}^2}} + E_E \frac{V_{sat,E}}{\sqrt{V_{sat,N}^2 + V_{sat,E}^2}}. \quad (27)$$

225 The footprints of the satellite observations at the altitude of the horizontal current sheet were traced along the IGRF field using the Apexpy code (Laundal et al., 2022b).

#### 2.4.2 Field-aligned current density

We also obtained Swarm single satellite (SW\_OPER\_FACxTMS\_2F) and dual-satellite (SW\_OPER\_FAC\_TMS\_2F) radial current measurements (“IRC”) (Ritter et al., 2013) as well as the auxiliaries “F107”, “SunZenithAngle”, and “MLT”. Field-aligned current amplitudes were mapped from the satellite altitude to the altitude of the horizontal current sheet by multiplying them by  $B_{IGRF,J_{DF}}/B_{IGRF,sat}$ , where the IGRF amplitude was obtained using Laundal et al. (2022b).

#### 2.5 All-sky camera data

We have used auroral images at 557.7 nm wavelength (green emission) from all-sky cameras (Kauristie, 2025) located at Sodankylä (SOD) and Kilpisjärvi (KIL) to observe auroral emission. The images are provided at a 20 s cadence, with an exposure time of 1 s. In order to compare with ionospheric currents, the auroral intensity was projected to 110 km (Partamies et al., 2022). Only elevation angles above  $70^\circ$  are included to cut out the parts with the largest positional uncertainty.

#### 2.6 Solar zenith angle, solar $F_{10.7}$ flux, and magnetic local time

We have calculated the solar zenith angle  $\chi$  using the pysolar code (Stafford, 2014). The solar  $F_{10.7}$  flux was obtained from [https://lasp.colorado.edu/lisird/data/penticton\\_radio\\_flux](https://lasp.colorado.edu/lisird/data/penticton_radio_flux). The magnetic local time (MLT) was calculated using the Apexpy code (Laundal et al., 2022b).



### 3 Results

#### 3.1 Statistical model

We assume that the ionospheric Hall ( $\Sigma_H$ ) and Pedersen ( $\Sigma_P$ ) conductances have two main components: a solar flux dependent part  $\Sigma_{EUV}$  and a precipitation dependent part  $\Sigma_{precip}$ ,

$$\Sigma = \sqrt{\Sigma_{BG}^2 + \Sigma_{EUV}^2 + \Sigma_{precip}^2}. \quad (28)$$

In addition, we assume a small constant background conductance  $\Sigma_{BG}$  (Ahn et al., 1998). The conductances are proportional to electron density, which in turn is proportional to the square root of the production rate. Because production rates can be summed up linearly (assuming that the conductivity types are generated at the same altitudes), different contributions to the conductance are summed up quadratically (cf., Janhunen et al., 2012).

Moen and Brekke (1993) have derived an empirical model for  $\Sigma_{EUV}$  as a function of the solar zenith angle  $\chi$  and solar  $F_{10.7}$  flux,

$$\Sigma_{P,EUV} = F_{10.7}^{0.49} (0.34 \cos \chi + 0.93 \cos^{1/2} \chi) \quad (29)$$

$$\Sigma_{H,EUV} = F_{10.7}^{0.53} (0.81 \cos \chi + 0.54 \cos^{1/2} \chi). \quad (30)$$

The distribution of  $\Sigma_P$  as observed by EISCAT as a function of  $\chi$  and  $F_{10.7}$  is illustrated in Figure 1. The left column shows the number of observations as a function of  $\chi$  (Fig. 1a) and  $F_{10.7}$  (Fig. 1c) and the right column shows the distributions of the observed values. The sum of values in each distribution column is 1, the thick white curve is the median, and the thin white curves are the 10, 25, 75, and 90 percentiles. The red curve is the median calculated using our new model (including both EUV and precipitation components as well as the constant background value, as will be explained in more detail below) and the blue curve is the median calculated using the Moen and Brekke (1993) empirical model (Eq. 29). Similar plots for  $\Sigma_H$  are shown in Figure 2. note that Eq. 29 and Eq. 30 do not describe the data particularly well as the conductances, especially  $\Sigma_P$ , are for instance overestimated in the lower range of  $\chi$ . Thus, we will make a new fit to the data using a modified formula,

$$\Sigma_{EUV} = c_1 F_{10.7}^{c_2} q'(\chi)^{c_3}, \quad (31)$$

where  $c_1$ – $c_3$  are the fitting parameters. The function  $q'(\chi)$  is the physically derived replacement for  $\cos(\chi)$  introduced by Laundal et al. (2022a) that describes EUV-associated plasma production. For our purposes, the main problem of using  $\cos(\chi)$  would be that the derivatives of  $\Sigma_{EUV}$  would become discontinuous at  $\chi = 90^\circ$ . Unlike  $\cos(\chi)$ ,  $q'(\chi)$  assumes that the Earth is not flat but round, and the resulting conductances do not have derivatives that go to negative infinity as  $\chi$  approaches  $90^\circ$  (Laundal et al., 2022a). A Python code for calculating  $q'(\chi)$  can be found as a supplement.

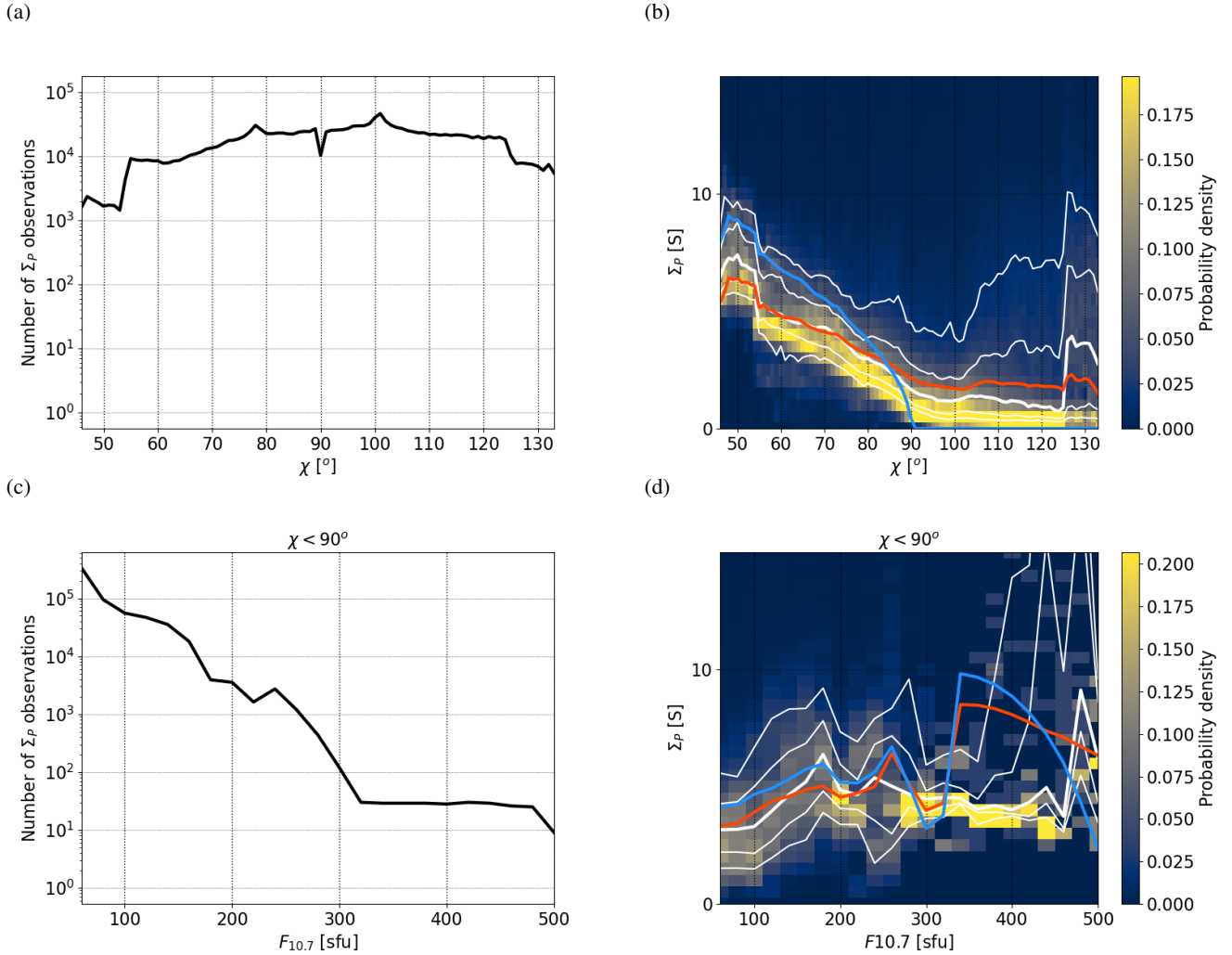


**Figure 1.** Number of EISCAT observations of the Pedersen conductance  $\Sigma_P$  as a function of the solar zenith angle  $\chi$  (a) and distribution of the observed  $\Sigma_P$  (b). For the distribution, the sum of values in each column is 1. The thick white curve is the median and the thin white curves are the 10, 25, 75, and 90 percentiles. The red curve is the median calculated using our new model, including both EUV and precipitation components, and the blue curve is the median calculated using the Moen and Brekke (1993) empirical model (Eq. 29). The bottom row shows corresponding data with  $\chi < 90^\circ$  as a function  $F_{10.7}$ .

Ahn et al. (1998) used Chatanika radar data to derive an empirical model for  $\Sigma_{precip}$  as a function of horizontal ( $\Delta H$ ) and vertical ( $\Delta Z$ ) ground magnetic field perturbations and magnetic local time (MLT). They used a relationship of the form

$$\Sigma = \begin{cases} a_1(MLT)|\Delta H|^{a_2(MLT)}, & \Delta H < 0, \Delta Z < 0 \\ a_3(MLT)|\Delta H|^{a_4(MLT)}, & \Delta H < 0, \Delta Z > 0 \\ a_5(MLT)|\Delta H|^{a_6(MLT)}, & \Delta H > 0, \Delta Z < 0 \\ a_7(MLT)|\Delta H|^{a_8(MLT)}, & \Delta H > 0, \Delta Z > 0 \end{cases}, \quad (32)$$

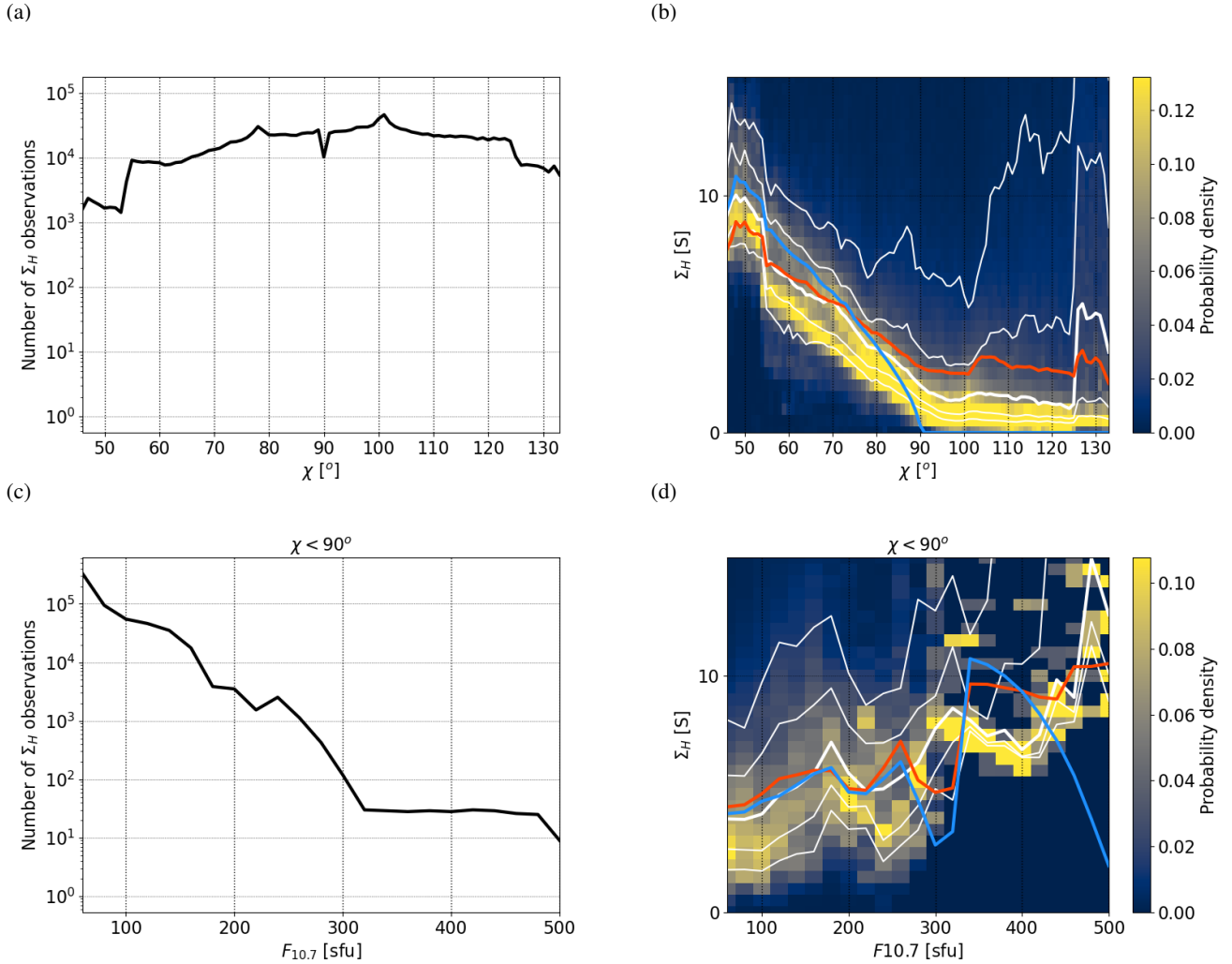


**Figure 2.** The same as Figure 1 except for the Hall conductance  $\Sigma_H$  instead of the Pedersen conductance  $\Sigma_P$ .

where the coefficients  $a(MLT)$  for different MLT sectors were determined by fitting the model to the observations. For the eastward electrojet region, the sectors were 13–15, 16–18, 19–21, 22–23, and 00–02 MLT and for the westward electrojet region, 19–21, 22–23, 00–02, 03–04, 05–06, 07–09, and 10–12 MLT.

We choose a similar approach, except that instead of  $|\Delta H|$  we use  $|\mathbf{J}_{DF}|$ . We use  $|\mathbf{J}_{DF}|$  instead of  $J_{eastward}$ , which would correspond to  $\Delta H$ , in order to avoid unphysical conductance structures when there is a  $\mathbf{J}_{DF}$  pattern more complicated than a basic electrojet.  $(\nabla \times \mathbf{J}_{DF})_r$  can be used as a proxy for the field-aligned current density under some conditions (see, e.g., Weygand and Wing, 2016; Juusola et al., 2023b), and higher conductance values might be expected for regions of upward field-aligned current than for downward field-aligned current. We tested using  $(\nabla \times \mathbf{J}_{DF})_r$  in a similar way as Ahn et al. (1998) used  $\Delta Z$ , but better results were obtained using  $|\mathbf{J}_{DF}|$  alone. Separate modelling of regions with positive and negative  $(\nabla \times \mathbf{J}_{DF})_r$



**Table 1.** Fitted values of the coefficients  $c_0$ – $c_3$  and their standard deviation (STD) errors from Eq. 31 ( $[F_{10.7}] = \text{sfu}$ ,  $[\Sigma_{EUV}] = \text{S}$ ) and from  $\Sigma_{BG} = c_0$  ( $[\Sigma_{BG}] = \text{S}$ ) for  $\Sigma_P$  and  $\Sigma_H$ .

	For $\Sigma_P$ :		For $\Sigma_H$ :	
	Value	STD error	Value	STD error
$c_0$	0.625	0.008	0.894	0.011
$c_1$	0.351	0.004	0.720	0.014
$c_2$	0.697	0.003	0.617	0.004
$c_3$	0.707	0.002	0.846	0.004

280 tended to give higher conductances for the region of negative  $(\nabla \times \mathbf{J}_{DF})_r$ , although opposite behavior is expected. The reason may be the limitation of  $(\nabla \times \mathbf{J}_{DF})_r$  for describing the location of possible conductance gradients.

Figure 3 shows  $\Sigma_P$  as a function of  $|\mathbf{J}_{DF}|$ ,  $(\nabla \times \mathbf{J}_{DF})_r$ , and MLT in a format similar to Fig. 1. Similar plots for  $\Sigma_H$  are displayed in Fig. 4. For our model, we use the expression

$$\Sigma_{precip} = c_4(MLT)|\mathbf{J}_{DF}|^{c_5(MLT)}. \quad (33)$$

285 Unlike Ahn et al. (1998), we do not try to distinguish between the eastward and westward electrojet region, because such a separation is not always unambiguous, e.g., when the current has a strong north-south component. The MLT dependence of the coefficients  $c_4$  and  $c_5$  will describe the different regions to some extent. The asymmetric distribution of the number of conductance observations for positive and negative  $(\nabla \times \mathbf{J}_{DF})_r$  in Fig. 3c and Fig. 4c may be related to the concentration of upward field-aligned current regions and the spreading of downward field-aligned current regions, as discussed for example by  
290 Yoshikawa et al. (2011).

The coefficients  $c_0$ – $c_5$ , where  $c_0 = \Sigma_{BG}$  is the constant background conductance, were determined by a least squares fit of the model to the observed  $\Sigma_P$  and  $\Sigma_H$ . The resulting values and standard deviation (STD) errors are provided in Tables 1–2. Linear interpolation was used for MLTs between those given in Table 2. The MLT-dependent coefficients  $c_4$ – $c_5$  are also illustrated in Figure 5. The coefficient pair  $c_4$  and  $c_5$  describe the precipitation dependence of  $\Sigma_P$  and  $\Sigma_H$ . In Fig. 5, both  
295 pairs display a general systematic tendency for the other coefficient to strengthen as the other weakens. Larger values of  $c_5$  indicate stronger dependence on  $|\mathbf{J}_{DF}|$ . Close to noon, the coefficient  $c_5$  is almost zero, which means that the conductance is almost independent of  $|\mathbf{J}_{DF}|$ . The conductance is also clearly larger than the background level ( $c_4 > c_0$ ). This is not caused by photoionisation, because it is included in the model. So, it seems that there must be precipitation that enhances the E region electron density but is not visible in  $|\mathbf{J}_{DF}|$ . A possible explanation are small-scale current systems that are not detected by  
300 ground-based magnetometers.

The correlation coefficient between the observed and modelled data is  $CC = 0.66$  for both  $\Sigma_P$  and  $\Sigma_H$ . The coefficient of determination

$$R^2 = 1 - \frac{\sum_i (\Sigma_i^{obs} - \Sigma_i^{mod})^2}{\sum_i (\Sigma_i^{obs} - \text{mean}(\Sigma^{obs}))^2} \quad (34)$$



**Table 2.** Fitted values of the MLT dependent coefficients  $c_4$  and  $c_5$  and their standard deviation (STD) errors from Eq. 33 ( $[|\mathbf{J}_{DF}|] = \text{A/km}$ ,  $[\Sigma_{precip}] = \text{S}$ ) for  $\Sigma_P$  and  $\Sigma_H$ .

MLT	For $\Sigma_P$ :		For $\Sigma_H$ :	
	$c_4$	$c_5$	$c_4$	$c_5$
00	0.272±0.004	0.564±0.003	0.184±0.003	0.757±0.003
01	0.212±0.004	0.602±0.003	0.248±0.004	0.702±0.003
02	0.268±0.004	0.565±0.003	0.256±0.005	0.705±0.003
03	0.357±0.006	0.507±0.003	0.343±0.006	0.649±0.003
04	0.241±0.005	0.578±0.003	0.344±0.006	0.652±0.003
05	0.225±0.005	0.598±0.004	0.341±0.007	0.662±0.003
06	0.283±0.006	0.538±0.004	0.285±0.007	0.683±0.004
07	0.621±0.013	0.338±0.005	0.676±0.013	0.453±0.004
08	1.185±0.026	0.175±0.006	1.617±0.035	0.236±0.005
09	1.643±0.037	0.075±0.007	2.610±0.058	0.115±0.006
10	1.756±0.042	0.011±0.007	2.818±0.064	0.079±0.007
11	1.562±0.041	0.000±0.009	2.962±0.064	0.042±0.007
12	1.421±0.042	0.000±0.010	2.579±0.066	0.035±0.008
13	1.327±0.038	0.037±0.009	2.049±0.066	0.030±0.010
14	1.001±0.029	0.164±0.008	1.367±0.053	0.126±0.011
15	0.959±0.022	0.222±0.006	0.701±0.027	0.306±0.009
16	0.672±0.014	0.314±0.005	0.277±0.011	0.529±0.008
17	0.300±0.007	0.470±0.004	0.141±0.006	0.653±0.008
18	0.150±0.004	0.645±0.005	0.081±0.003	0.811±0.006
19	0.241±0.005	0.581±0.004	0.172±0.004	0.710±0.005
20	0.253±0.005	0.587±0.003	0.178±0.004	0.753±0.004
21	0.340±0.005	0.533±0.003	0.223±0.004	0.721±0.003
22	0.391±0.005	0.504±0.003	0.322±0.005	0.657±0.003
23	0.413±0.005	0.498±0.002	0.373±0.005	0.635±0.002

is  $R^2 = 0.43$  for  $\Sigma_P$  and  $R^2 = 0.44$  for  $\Sigma_H$ . Considering that the scale sizes of IMAGE-based  $\mathbf{J}_{DF}$  and EISCAT-based conductances are different, meso-scale and small-scale, respectively, these numbers seem reasonable. The thick white and red curves in Fig. 1–4 show the median of the observed and modelled values, respectively. Generally, the white and red curves follow each other relatively well, and in Fig. 1b and Fig. 2b, the red curves fit the data better than the Moen and Brekke (1993) model (blue curves). The wrong dependence on  $(\nabla \times \mathbf{J}_{DF})_r$ , discussed above, is also visible in the median curves of the observed and modelled data in Fig. 3d and Fig. 4d.



Figure 6 shows the observed  $\Sigma_P$  (top),  $\Sigma_H$  (middle), and Hall-to-Pedersen conductance ratio  $\alpha = \frac{\Sigma_H}{\Sigma_P}$  (bottom) as a function of the modelled value in a format similar to Fig. 1–4. The red curves in the right column are lines of unity. The median curve aligns well with the line of unity for all three parameters, indicating good agreement between observed and modelled values.

A summary of fitting the model is displayed on the left hand side of Figure 7. The right hand side illustrates how the model is used in section 3.2 (“Option a”) and section 3.3 (“Option b”).

### 3.2 Comparison with the SWIPE model

In order to start validating the new empirical conductance model, we will apply it to  $|J_{DF}|$  from the Average Magnetic field and Polar current System (AMPS) model (Laundal et al., 2018) and compare with the Swarm Ionospheric Polar Electrodynamics (SWIPE) model (Hatch et al., 2024) conductances for the same conditions. AMPS is a climatological model of polar ionospheric currents, based on magnetic field measurements from the CHAMP and Swarm satellites, and SWIPE is a climatological model of polar ionospheric electrodynamics, based on the Thermal Ion Imager (TII) and Vector Field Magnetometer (VFM) instruments carried by Swarm.

Because SWIPE has not been very extensively validated, we will first compare the SWIPE conductances with EISCAT observations. Figure 8 is otherwise the same as Fig. 6a–d except that instead of the new EISCAT-based model, values modelled using SWIPE are compared with the EISCAT observations. The solar wind speed and interplanetary magnetic field data propagated to Earth’s bow shock nose that were needed as input for SWIPE were extracted from NASA/GSFC’s OMNI data set through OMNIWeb (Papitashvili and King, 2020). We have not included SWIPE conductances that should be masked according to the criteria specified in Hatch et al. (2024) ( $\mathbf{J} \cdot \mathbf{E} < 0.5 \text{ mW/m}^2$ ;  $\Sigma \leq 0 \text{ S}$ ). Fig. 8 shows that there is reasonable agreement between SWIPE and EISCAT for small conductance values.

Figure 9a shows  $|J_{DF}|$  from AMPS as a function of magnetic latitude and MLT for dipole tilt angle  $0^\circ$  (equinox), solar wind speed  $V = 450 \text{ km/s}$ ,  $F_{10.7} = 120 \text{ sfu}$ , Interplanetary Magnetic Field (IMF)  $B_{GSM,y} = 0 \text{ nT}$  and  $B_{GSM,z} = -5 \text{ nT}$ . For reference, we also show contours of the field-aligned current density from AMPS. Fig. 9b and Fig. 9c show the conductances estimated using our model, and Fig. 9d and Fig. 9e show the conductances from the SWIPE model for the same conditions as those applied to the AMPS model. There are some white areas in the modelled conductances, because SWIPE can only produce conductance estimates when the conductances are “electrodynamically visible”. That is, if  $\mathbf{J}$  and  $\mathbf{E}$  are not large enough or if  $\mathbf{J} \cdot \mathbf{E} < 0$ , the conductances cannot be estimated. As a result, SWIPE conductances have a baseline uncertainty of at least  $0.5 \text{ S}$  (Hatch et al., 2024).

Both SWIPE and AMPS-EISCAT conductances show the highest values in the midnight and morning sector auroral oval. For SWIPE, the maximum of  $\Sigma_P$  is around midnight and of  $\Sigma_H$  around 3 MLT, whereas for AMPS-EISCAT the entire post-midnight sector shows increased values. The maximum amplitude of the AMPS-EISCAT  $\Sigma_H$  (15 S) is somewhat higher than that of SWIPE (12 S) whereas the maximum amplitude of the AMPS-EISCAT  $\Sigma_P$  (7 S) is slightly lower than that of SWIPE (9 S).

Next, we solve Eq. 24 for  $Q_{CF,i}$  using  $\Sigma_P$  from Fig. 9b,  $\Sigma_H$  from Fig. 9c, and  $I_{DF,i}$  from AMPS  $(\nabla \times \mathbf{J}_{DF})_r$  according to Eq. 9. AMPS  $(\nabla \times \mathbf{J}_{DF})_r$  is shown in Figure 10a. The red and blue field-aligned current density contours in Fig. 10a are based



on AMPS data and identical to those in Fig. 9.  $E_{DF}$  is assumed to be negligible.  $I_{CF}$  is then determined using Eq. 25. We have  
 345 used a triangular grid and only included triangles where all nodes have latitudes  $\geq 60^\circ$ . The values of  $|\mathbf{J}_{DF}|$ ,  $(\nabla \times \mathbf{J}_{DF})_r$ ,  $\Sigma_P$ ,  
 and  $\Sigma_H$  were first calculated for the grid nodes. The conductance gradients and values for the triangle faces were estimating  
 using the finite difference approach

$$\nabla \Sigma_{\theta, face} = \frac{\Sigma_{node2} - \Sigma_{node1}}{R(\theta_{node2} - \theta_{node1})} \quad (35)$$

$$\nabla \Sigma_{\phi, face} = \frac{\Sigma_{node2} - \Sigma_{node1}}{R \sin \theta_{face} (\phi_{node2} - \phi_{node1})} \quad (36)$$

$$350 \quad \Sigma_{face} = \frac{\Sigma_{node1} + \Sigma_{node2} + \Sigma_{node3}}{3} \quad (37)$$

$$A_{face} = R^2 \cdot (C_{node1, node2} + C_{node2, node3} + C_{node3, node1} - \pi), \quad (38)$$

where the triangle cell area  $A$  in Eq. 24 and Eq. 25 was calculated from the excess of the triangle angles  $C$ . The two out of three  
 nodes used to calculate the gradients were selected to yield the largest latitude and longitude variations across the triangle. The  
 face grid was used to solve Eq. 24 and Eq. 25. The resulting field-aligned current density and electric potential are displayed  
 355 in Fig. 10b and c. The corresponding distributions from AMPS and SWIPE are illustrated in Fig. 10d and Fig. 10e.

AMPS (Fig. 10d) shows the expected pattern of Region 1 and Region 2 field-aligned current rings. In the dusk sector, the  
 pattern and amplitudes produced by AMPS-EISCAT (Fig. 10b) are quite similar. In the dawn sector, the direction of the field-  
 aligned current density more or less agrees with AMPS, but the amplitude is clearly weaker. SWIPE (Fig. 10e) shows the  
 expected two-cell convection pattern with a potential difference of 93 kV. AMPS-EISCAT (Fig. 10c) also produces a two-cell  
 360 convection pattern, but the potential drop is smaller, 77 kV. The difference can be explained by the higher Hall conductance of  
 the AMPS-EISCAT model (Fig. 9c) compared to the SWIPE model (Fig. 9e).

### 3.3 Combining IMAGE observations and the empirical conductance model

In this section we will apply the new empirical conductance model to solve Eq. 24 for  $Q_{CF,i}$  when  $I_{DF,i}$  and  $E_{DF}$  have been  
 determined by applying the 2D SECS method to IMAGE magnetic field observations.  $I_{CF}$  is then determined using Eq. 25.  
 365 First, we determine  $\Sigma_P$  and  $\Sigma_H$  from the known  $\mathbf{J}_{DF}$ ,  $F_{10.7}$ ,  $\chi$ , and MLT, as described in Section 3.1. The conductance  
 gradients and conductances at the same locations are then estimated using the finite difference approach,

$$\nabla \Sigma_{\theta, i+\frac{1}{2}, j+\frac{1}{2}} = \frac{1}{2} \cdot \left( \frac{\Sigma_{i+1, j} - \Sigma_{i, j}}{R \Delta \theta} + \frac{\Sigma_{i+1, j+1} - \Sigma_{i, j+1}}{R \Delta \theta} \right) \quad (39)$$

$$\nabla \Sigma_{\phi, i+\frac{1}{2}, j+\frac{1}{2}} = \frac{1}{2} \cdot \left( \frac{\Sigma_{i, j+1} - \Sigma_{i, j}}{R \sin \theta_{\phi, i+\frac{1}{2}, j+\frac{1}{2}} \Delta \phi} + \frac{\Sigma_{i+1, j+1} - \Sigma_{i+1, j}}{R \sin \theta_{\phi, i+\frac{1}{2}, j+\frac{1}{2}} \Delta \phi} \right) \quad (40)$$

$$\Sigma_{i+\frac{1}{2}, j+\frac{1}{2}} = \frac{\Sigma_{i, j} + \Sigma_{i+1, j} + \Sigma_{i, j+1} + \Sigma_{i+1, j+1}}{4} \quad (41)$$

$$370 \quad A_{i+\frac{1}{2}, j+\frac{1}{2}} = 2R^2 \Delta \phi \sin \theta_{i+\frac{1}{2}, j+\frac{1}{2}} \sin \frac{\Delta \theta}{2}. \quad (42)$$

Here,  $A$  is the grid cell area in Eq. 24 and Eq. 25,  $\Delta \theta$  is the co-latitude grid resolution, and  $\Delta \phi$  is the longitude grid resolution  
 for the rectangular grid.

Figure 11 shows an example of the application of the 2D SECS method to IMAGE magnetic field data. Fig. 11a displays  
 $\mathbf{J}_{DF}$  (arrows) and  $(\nabla \times \mathbf{J}_{DF})_z = -(\nabla \times \mathbf{J}_{DF})_r$  (color) as a function of geographic latitude and longitude on 31 August 2014



375 at 23:10:00 UT (Juusola et al., 2016a). Locations of the IMAGE stations used in the analysis are indicated by the red circles and Apex coordinates (Richmond, 1995; Emmert et al., 2010; Laundal et al., 2022b) with the blue grid. The event took place in the post-midnight sector, around 01 MLT. The SOD all-sky camera field-of-view is indicated by the black circle and the track of Swarm A by the black line.  $\mathbf{J}_{DF}$  shows a westward electrojet. Fig. 11b illustrates the external part of  $\mathbf{E}_{DF}$  due to time-varying ionospheric currents, Fig. 11c internal part of  $\mathbf{E}_{DF}$  due to time-varying telluric currents (Juusola et al., 2024),  
380 and Fig. 11d the total  $\mathbf{E}_{DF}$ .  $\mathbf{E}_{DF}$  is displayed by the vectors and  $(\nabla \times \mathbf{E}_{DF})_z$  by the color. The values are small due to the stationarity of the event.

Fig. 11e shows the auroral intensity from the SOD all-sky camera mapped to 110 km altitude. There is an auroral arc between  $66.0^\circ$  and  $66.5^\circ$  latitude, in the middle of the westward electrojet. The arrows in Fig. 11f–g repeat  $\mathbf{J}_{DF}$ , and the color shows  $\Sigma_P$  and  $\Sigma_H$  estimated from  $\mathbf{J}_{DF}$  and MLT. This is a nightside event for which  $\Sigma_{EUV} = 0$ .

385 Fig. 11h displays  $\mathbf{E}_{CF}$  (arrows) and its divergence ( $\nabla \cdot \mathbf{E}_{CF}$ , color), Fig. 11i  $\mathbf{J}_{CF}$  (arrows) and its divergence ( $\nabla \cdot \mathbf{J}_{CF} = j_z = -j_r$ , color), Fig. 11j the total horizontal ionospheric current density ( $\mathbf{J} = \mathbf{J}_{DF} + \mathbf{J}_{CF}$ , arrows) and its divergence ( $\nabla \cdot \mathbf{J} = j_z = -j_r$ , color), and Fig. 11k the dot product between the total horizontal current density and electric field ( $\mathbf{J} \cdot \mathbf{E}$ ) as a proxy for Joule heating. Any negative values of  $\mathbf{J} \cdot \mathbf{E}$  indicate a dynamo. The gray curves illustrate contours of the electric potential (derived using Eq. 23), and the potential difference between the maximum and minimum, indicated by the gray crosses, is  
390 written in the top left corner of each panel.

There is upward current (negative  $\nabla \cdot \mathbf{J}_{CF}$  in Fig. 11i) in the region where Fig. 11e shows the auroral arc and more diffuse emission south of the arc. North of the arc, in the region where there is no auroral emission, the field-aligned current is downward, as expected. The electric field in Fig. 11h is directed southward and maximizes north of the arc. This configuration of the field-aligned currents and electric field is typical for a morning sector auroral arc (e.g., Juusola et al., 2016a).  $\mathbf{J} \cdot \mathbf{E}$  in  
395 Fig. 11k maximizes in the middle of the westward electrojet.

Similar plots for an evening sector auroral arc, observed by the KIL all-sky camera, are shown in Figure 12. This time, the arc is located in the middle of an eastward electrojet. There is upward current (Fig. 12i) at the location of the arc (Fig. 12e), more diffuse downward current south of the arc, and an enhanced northward electric field (Fig. 12h) south of the arc, as expected for an evening sector auroral arc (Aikio et al., 2002).  $\mathbf{J} \cdot \mathbf{E}$  in Fig. 12k maximizes in the middle of the eastward electrojet.

### 400 3.4 Comparison with Swarm observations

In order to validate both the empirical model and the solver, we compare the electric field and radial current derived from IMAGE data to those observed by Swarm A and C satellites as they crossed IMAGE. Figure 13 illustrates four example crossings, including the two auroral arc crossings of the previous section. For each crossing, the three panels from top to bottom show the electric field as observed by Swarm A (black) and the electric field component parallel to the Swarm A track modelled based on IMAGE observations (red). The middle panel shows the single satellite radial current from Swarm A (black; scale on the left), dual satellite radial current from Swarm A and C (blue; scale on the right), and radial current modelled based on IMAGE observations (red; scale on the right). The bottom panel shows the solar zenith angle  $\chi$  (black; scale on the left) and MLT (blue; scale on the right). The  $F_{10.7}$  flux value during the crossing is indicated in the bottom panel as well. The  
405



shaded region indicates a large gap in the IMAGE magnetometer latitude coverage. The key curves in Fig. 13a and d will be discussed in Section 4.2.

The two crossings in the top row took place in darkness ( $\chi > 90^\circ$ ), such that  $\Sigma_{EUV} = 0$ , and the two crossing in the bottom row took place in sunlight ( $\chi < 90^\circ$ ), such that  $\Sigma_{EUV} > 0$ . In all four events, the IMAGE-based electric field estimate (red) has a reasonably similar profile as the large-scale Swarm observation, but the amplitude is weaker, especially for the post-midnight sector auroral oval crossings (Fig. 13a and d). There is a reasonable agreement on the direction of the large-scale radial current from Swarm A and C and IMAGE.



## 4 Discussion

### 4.1 Limitations of the conductance model

The precipitation component of our conductance model is parametrized with the divergence-free component of the horizontal ionospheric current density. In addition to the auroral oval,  $|\mathbf{J}_{DF}|$  generally has a significant value in the polar cap as well. In the dark polar cap,  $\mathbf{J}_{DF}$  and  $\mathbf{J}_{CF}$  tend to oppose each other, summing up to almost zero (Laundal et al., 2018). Thus, while  $\Sigma_{EUV}$  is in principle expected to be valid everywhere,  $\Sigma_{precip}$  is not valid inside the polar cap. Examination of the global maps in Fig. 9 clearly shows that the values given by our model for the polar cap are too large. The model by Ahn et al. (1998) had the same limitation. They noted that conductances in the dark polar cap are very low,  $\Sigma_H < 2.0$  S and  $\Sigma_P < 1.0$  S (Fuller-Rowell and Evans, 1987), and not particularly sensitive to geomagnetic activity. Conductances in the sunlit polar cap, on the other hand, are dominated by  $\Sigma_{EUV}$ . Thus, an improvement to our model would be to try to identify the boundary between auroral oval and polar cap from  $\mathbf{J}_{DF}$  and apply the fitted constant background values ( $c_0$  in Table 1) to that region.

Our EISCAT data set contains observations not only from the auroral oval but from the polar cap and subauroral region as well. Our modeling assumes that  $|\mathbf{J}_{DF}|$  is zero outside the auroral oval, which is not true and introduces some error to the model. Furthermore, we assume that the conductances have similar profiles as the meso-scale  $|\mathbf{J}_{DF}|$ . The meso-scale conductivity profiles derived from Swarm data by Juusola et al. (2016a) for a single event appear to be in agreement with this. However, the small-scale  $\Sigma_P$  profile deviates from the meso-scale  $|\mathbf{J}_{DF}|$ . Ritter et al. (2004) have shown that small-scale field-aligned currents typically occur in the middle of the westward electrojet. It is possible that there should be corresponding small-scale structure in  $\mathbf{J}_{DF}$  as well, but ground magnetometers or Swarm are not able to distinguish it. The same applies to the dayside, where our model predicts  $\Sigma_{precip}$  values that are clearly larger than the background level but almost independent of  $|\mathbf{J}_{DF}|$ , as discussed in section 3.1. The Electrojet Zeeman Imaging Explorer (EZIE) mission (e.g., Laundal et al., 2021; Yee et al., 2021b, a) can help to clarify this.



### 4.2 Possible role of conductance gradients in the post-midnight sector

As demonstrated by Fig. 10 and Fig. 13, the electric field and field-aligned current density solved using the conductance model tend to be suppressed in the post-midnight sector where the conductances are high. Reducing the peak amplitudes of the




conductances significantly, to the same level as in the pre-midnight section, would increase the electric field and field-aligned current density, but this does not agree with the observations. Another possibility is to introduce conductance gradients to the model. As mentioned in section 3.1, fitting the conductance data set with separate coefficients for the regions of positive and negative  $(\nabla \times \mathbf{J})_r$  failed. We speculated that this may have been due to the limitation of  $(\nabla \times \mathbf{J})_r$  to describe the location of the conductance gradient.

We will test the effects of conductance gradients for the two postmidnight crossings shown in Fig. 13a and d. In both cases, Swarm observes a sharp electric field intensification at geographic latitude  $66^\circ$ . We artificially produce sharp conductance gradients at this location by multiplying  $\Sigma_{precip}$  poleward of  $66^\circ$  latitude by 0.2 (crossing in Fig. 13a) or 0.1 (crossing in Fig. 13d). The multipliers were selected to produce an electric field intensification visually matching that observed by Swarm. We tested using the sign change of  $(\nabla \times \mathbf{J})_r$  instead of the  $66^\circ$  latitude threshold, but the resulting electric field intensifications were offset from those observed by Swarm.


The effect of the conductance gradients on the electric field and field-aligned current density is illustrated by the grey curves in the top and middle panels of Fig. 13a and d. The upward field-aligned current density forms a narrow intensification at the location of the conductance gradient. For the crossing of Fig. 13a, this coincides with the auroral arc, as illustrated in Figure 14, in a format similar to Fig. 11. Panels 14a–e are identical to those in Fig. 11, but they are repeated for easier comparison. As intended, the modified conductances (Fig. 14f–g) are smaller in the poleward part of the electrojet compared to the original ones (Fig. 11f–g). The field-aligned current (Fig. 14i) is modified such that there is now a concentrated upward current (blue) at the location of the auroral arc and more diffuse downward current north of the arc. The electric field (Fig. 14h) is modified such that now there is a step-like enhancement of the southward directed electric field immediately north of the arc. A similar step-like enhancement is reflected in  $\mathbf{J} \cdot \mathbf{E}$  (Fig. 14k).


Our results suggest a possible mechanism that may contribute to the formation of auroral arcs in the post-midnight sector: As the horizontal current that connects the large-scale field-aligned currents created by the magnetosphere flows across ionospheric conductance gradients, the ionosphere actively modifies the field-aligned current distribution and creates concentrated upward field-aligned currents at the conductance gradients. This active role of the ionosphere would explain why the magnetospheric processes that drive arcs are not fully understood (Borovsky et al., 2020). It is also in agreement with the suggestion by Newell et al. (1996, 1998) that ionospheric conductivity is the key factor controlling the occurrence of discrete auroras. The steady, hemispherically conjugate conductance gradient structure at the boundary between the large-scale Region 1 and Region 2 field-aligned currents agrees with the highly east-west elongated form of the auroral arcs, their conjugate appearance on closed field lines, and the observation that they can remain stable for tens of minutes (Karlsson et al., 2020; Borovsky et al., 2020). The weakening of the conductance gradient in the dayside agrees with the observed suppression of discrete auroras by sunlight and the observation that the occurrence rate of intense auroras is uncorrelated with solar activity in darkness (Newell et al., 1996, 1998). The large  $\nabla \cdot \mathbf{E}$  within the arc in Fig. 12 and the associated electric field pattern agrees with the expectation that there should be polarization charges within the arc, even though the electric field remains small on one side of the arc (de la Beaujardière et al., 1981).



Global simulations generally determine the ionospheric electric potential from the given field-aligned current distribution and ionospheric conductances. The problem with this approach may be that the ionosphere is not allowed to directly modify the field-aligned current distribution. Thus, the small-scale structures leading to auroral arcs will never be modelled regardless of the grid resolution. 

## 5 Conclusions

We have used all available field-aligned observations from the EISCAT UHF radar since 2001 and from the 42 m ESR radar since 1998 to develop a new empirical model for estimating the high-latitude ionospheric Hall and Pedersen conductances. Following Moen and Brekke (1993), the solar radiation components were parametrized with the solar zenith angle and the  $F_{10.7}$  index. Following Ahn et al. (1998), the auroral precipitation components were parametrized with the magnetic local time (MLT) and the divergence-free part of the horizontal ionospheric current density  $\mathbf{J}_{DF}$ , which was derived from ground-based magnetic field observations. Both models were fitted to the observations simultaneously. The model is described by Eqs 28, 31, and 33 and the fitted coefficients are provided in Tables 1 and 2. Comparison of the new model with a climatological conductance model showed reasonable agreement. We will call the new model “Ebec” for **EISCAT-based empirical conductance model**. 

We have also derived a new SECS-based technique for solving the ionospheric potential electric field and field-aligned current density from known ionospheric conductances,  $\mathbf{J}_{DF}$ , and the inductive electric field  $\mathbf{E}_{DF}$ . Similar to  $\mathbf{J}_{DF}$ ,  $\mathbf{E}_{DF}$  can be obtained from ground-based magnetic field observations. Juusola et al. (2024) have shown that  $\mathbf{E}_{DF}$  has both a significant external contribution due to time-varying ionospheric currents and a significant internal contribution due to time-varying telluric currents. Our technique takes both into account. Vanhamäki et al. (2007) and Madelaire et al. (2024) have shown that in dynamical situations,  $\mathbf{E}_{DF}$  is not negligible. The new empirical conductance model and solver were applied to ground-based IMAGE magnetic field observations. Comparison of the results with simultaneous Swarm observations showed reasonable agreement in the electric field profile and direction of the field-aligned current, but in the post-midnight region of large conductances, the amplitudes tended to be weaker than those observed by Swarm. More research is needed to understand the ionospheric conductances better, but we hope that meanwhile the combination of the new conductance model and analysis technique can help in studies of ionospheric electrodynamics. 

*Code and data availability.* The data from EISCAT (Madrigal, 2025), IMAGE (Juusola et al., 2025), and Swarm (VirES, 2025) and the Solar Radio Flux at 10.7 cm (NRC, 2025) are freely available. All-sky camera data are available on request from Kirsti Kauristie (kirsti.kauristie@fmi.fi). Solar wind data were extracted from NASA/GSFC’s OMNI data set through OMNIWeb <https://omniweb.gsfc.nasa.gov/>. The code for the SECS method is available as a supplement to Vanhamäki and Juusola (2020). The codes Apexpy (Laundal et al., 2022b), pysolar (Stafford, 2014), AMPS (Laundal, 2024), SWIPE (Hatch, 2024), Guisdap (Häggström, 2025), and VirES-Python-Client (Smith et al., 2025) are freely available. A Python code for calculating the cosine alternative  $q'(\chi)$  is provided as a supplement to this paper.



*Author contributions.* LJ implemented the method and prepared the manuscript and IV processed the EISCAT data. SMH has derived the function  $q'(\chi)$  and the SWIPE model and provided expertise on using them. He has also written the Python code for calculating  $q'(t)$  that is provided as a supplement. MG and NP provided expertise in auroral observations and physics, HV in ionospheric electrodynamics, and AW and UG in ionosphere modelling. IH implemented the triangle grid. All co-authors participated in writing the manuscript.

*Competing interests.* MP is a member of the editorial board of Annales Geophysicae. Otherwise, the authors declare that they have no conflict of interest.

*Acknowledgements.* We thank EISCAT for the incoherent scatter radar data. EISCAT is an international association supported by research organisations in China (CRIRP), Finland (SA), Japan (NIPR and ISEE), Norway (NFR), Sweden (VR), and the United Kingdom (UKRI). We thank the institutes who maintain the IMAGE Magnetometer Array: Tromsø Geophysical Observatory of UiT the Arctic University of Norway (Norway), Finnish Meteorological Institute (Finland), Institute of Geophysics Polish Academy of Sciences (Poland), GFZ German Research Centre for Geosciences (Germany), Geological Survey of Sweden (Sweden), Swedish Institute of Space Physics (Sweden), Sodankylä Geophysical Observatory of the University of Oulu (Finland), Polar Geophysical Institute (Russia), DTU Technical University of Denmark (Denmark), and Science Institute of the University of Iceland (Iceland). The provisioning of data from AAL, GOT, HAS, NRA, VXJ, FKP, ROE, BFE, BOR, HOV, SCO, KUL, and NAQ is supported by the ESA contracts number 4000128139/19/D/CT as well as 4000138064/22/D/KS. We acknowledge use of NASA/GSFC's Space Physics Data Facility's OMNIWeb service, and OMNI data. This research was supported by the Research Council of Finland projects no. 347795, 347796, 354521, 360433, and 352846. SMH was supported by the Norwegian Research Council under contract 344061.



## References

- Ahn, B.-H., Richmond, A. D., Kamide, Y., Kroehl, H. W., Emery, B. A., de la Beaujardiére, O., and Akasofu, S.-I.: An ionospheric conductance model based on ground magnetic disturbance data, *J. Geophys. Res.*, 103(A7), 14 769–14 780, <https://doi.org/https://doi.org/10.1029/97JA03088>, 1998.
- 525 Aikio, A. T., Lakkala, T., Kozlovsky, A., and Williams, P. J. S.: Electric fields and currents of stable drifting auroral arcs in the evening sector, *J. Geophys. Res.*, 107(A12), 1424, <https://doi.org/https://doi.org/10.1029/2001JA009172>, 2002.
- Alken, P., Thébault, E., Beggan, C. D., Amit, H., Aubert, J., Baerenzung, J., Bondar, T. N., Brown, W. J., Califf, S., Chambodut, A., Chulliat, A., Cox, G. A., Finlay, C. C., Fournier, A., Gillet, N., Grayver, A., Hammer, M. D., Holschneider, M., Huder, L., Hulot, G., Jager, T., Kloss, C., Korte, M., Kuang, W., Kuvshinov, A., Langlais, B., Léger, J.-M., Lesur, V., Livermore, P. W., Lowes, F. J., Macmillan, S.,
- 530 Magnes, W., Manda, M., Marsal, S., Matzka, J., Metman, M. C., Minami, T., Morschhauser, A., Mound, J. E., Nair, M., Nakano, S., Olsen, N., Pavón-Carrasco, F. J., Petrov, V. G., Ropp, G., Rother, M., Sabaka, T. J., Sanchez, S., Saturnino, D., Schnepf, N. R., Shen, X., Stolle, C., Tangborn, A., Tøffner-Clausen, L., Toh, H., Torta, J. M., Varner, J., Vervelidou, F., Vigneron, P., Wardinski, I., Wicht, J., Woods, A., Yang, Y., Zeren, Z., and Zhou, B.: International Geomagnetic Reference Field: the thirteenth generation, *Earth Planets Space*, 73, <https://doi.org/https://doi.org/10.1186/s40623-020-01288-x>, 2021.
- 535 Amm, O.: Ionospheric elementary current systems in spherical coordinates and their application, *J. Geomagn. Geoelectr.*, 49, 947–955, <https://doi.org/https://doi.org/10.5636/jgg.49.947>, 1997.
- Amm, O. and Viljanen, A.: Ionospheric disturbance magnetic field continuation from the ground to ionosphere using spherical elementary current systems, *Earth Planets Space*, 51, 431–440, <https://doi.org/https://dx.doi.org/10.1186/BF03352247>, 1999.
- Anderson, B. J., Takahashi, K., Kamei, T., Waters, C. L., and Toth, B. A.: Birkeland current system key parameters derived from Iridium observations: Method and initial validation results, *J. Geophys. Res.*, 107(A6), <https://doi.org/https://doi.org/10.1029/2001JA000080>, 2002.
- 540 Baloukdis, D., Sarris, T., Tourgaidis, S., Pirnaris, P., Aikio, A., Virtanen, I., and S. Buchert, K. P.: A comparative assessment of the distribution of Joule heating in altitude as estimated in TIE-GCM and EISCAT over one solar cycle, *Journal of Geophysical Research: Space Physics*, 128, e2023JA031 526, <https://doi.org/https://doi.org/10.1029/2023JA031526>, 2023.
- 545 Bilitza, D., Pezzopane, M., Truhlik, V., Altadill, D., Reinisch, B. W., and Pignalberi, A.: The International Reference Ionosphere model: A review and description of an ionospheric benchmark, *Reviews of Geophysics*, 60, e2022RG000 792, <https://doi.org/https://doi.org/10.1029/2022RG000792>, 2022.
- Borovsky, J. E., Birn, J., Echim, M. M., Fujita, S., Lysak, R. L., Knudsen, D. J., Marghitu, O., Otto, A., Watanabe, T.-H., and Tanaka, T.: Quiescent Discrete Auroral Arcs: A Review of Magnetospheric Generator Mechanisms, *Space Sci. Rev.*, 216, <https://doi.org/https://doi.org/10.1007/s11214-019-0619-5>, 2020.
- 550 Burchill, J. and Knudsen, D.: EFI TII Cross-Track Flow Data Release Notes, <https://earth.esa.int/eogateway/documents/20142/37627/swarm-EFI-TII-cross-track-flow-dataset-release-notes.pdf>, last access: May 27, 2025, 2020.
- Chisham, G., Lester, M., Milan, S. E., Freeman, M. P., Bristow, W. A., Grocott, A., McWilliams, K. A., Ruohoniemi, J. M., Yeoman, T. K., Dyson, P. L., Greenwald, R. A., Kikuchi, T., Pinnock, M., Rash, J. P. S., Sato, N., Sofko, G. J., Villain, J.-P., and Walker, A. D. M.: A decade of the Super Dual Auroral Radar Network (SuperDARN): scientific achievements, new techniques and future directions, *Surv. Geophys.*, 28, 33–109, <https://doi.org/https://doi.org/10.1007/s10712-007-9017-8>, 2007.



- de la Beaujardière, O., Vondrak, R., Heelis, R., Hanson, W., , and Hoffman, R.: Auroral arc electrodynamic parameters measured by AE-C and the Chatanika Radar, *J. Geophys. Res.*, 86(A6), 4671–4685, <https://doi.org/https://doi.org/10.1029/JA086iA06p04671>, 1981.
- Emmert, J. T., Richmond, A. D., and Drob, D. P.: A computationally compact representation of Magnetic-Apex and Quasi-Di pole coordinates with smooth base vectors, *J. Geophys. Res.*, 115, A08322, <https://doi.org/https://doi.org/10.1029/2010JA015326>, 2010.
- Fuller-Rowell, T. J. and Evans, D. S.: Height-integrated Pedersen and Hall conductivity patterns inferred from the TIROS-NOAA satellite data, *J. Geophys. Res.*, 92(A7), 7606–7618, <https://doi.org/https://doi.org/10.1029/JA092iA07p07606>, 1987.
- Gjerloev, J. W.: The SuperMAG data processing technique, *J. Geophys. Res.*, 117, A09213, <https://doi.org/https://doi.org/10.1029/2012JA017683>, 2012.
- Green, D. L., Waters, C. L., Korth, H., Anderson, B. J., Ridley, A. J., and Barnes, R. J.: Technique: Large-scale ionospheric conductance estimated from combined satellite and ground-based electromagnetic data, *J. Geophys. Res.*, 112, A05303, <https://doi.org/https://doi.org/10.1029/2006JA012069>, 2007.
- Hägström, I.: Guisdap 9.2 [code], <https://gitlab.com/eiscat/guisdap9>, last access: May 27, 2025, 2025.
- Hatch, S. M.: Python interface for the Swarm Ionospheric Polar Electrodynamics (SWIPE) model [code], <https://github.com/Dartspacephysiker/pyswipe>, last access: May 27, 2025, 2024.
- Hatch, S. M., Vanhamäki, H., Laundal, K. M., Reistad, J. P., Burchill, J. K., Lomidze, L., Knudsen, D. J., Madelaire, M., and Tesfaw, H.: Does high-latitude ionospheric electrodynamics exhibit hemispheric mirror symmetry?, *Ann. Geophys.*, 42, 229–253, <https://doi.org/https://doi.org/10.5194/angeo-42-229-2024>, 2024.
- Ieda, A., Oyama, S., Vanhamäki, H., Fujii, R., Nakamizo, A., Amm, O., Hori, T., Takeda, M., Ueno, G., Yoshikawa, A., Redmon, R. J., Denig, W. F., Kamide, Y., and Nishitani, N.: Approximate forms of daytime ionospheric conductance, *J. Geophys. Res. Space Physics*, 119, 10397–10415, <https://doi.org/https://doi.org/10.1002/2014JA020665>, 2015.
- Janhunen, P., Palmroth, M., Laitinen, T., Honkonen, I., Juusola, L., Facskó, G., and Pulkkinen, T.: The GUMICS-4 global MHD magnetosphere–ionosphere coupling simulation, *Journal of Atmospheric and Solar-Terrestrial Physics*, 80, 48–59, <https://doi.org/https://doi.org/10.1016/j.jastp.2012.03.006>, 2012.
- Juusola, L., Archer, W. E., Kauristie, K., Burchill, J. K., Vanhamäki, H., and Aikio, A. T.: Ionospheric conductances and currents of a morning sector auroral arc from Swarm-A electric and magnetic field measurements, *Geophys. Res. Lett.*, 43, 11519–11527, <https://doi.org/https://doi.org/10.1002/2016GL070248>, 2016a.
- Juusola, L., Kauristie, K., Vanhamäki, H., and Aikio, A.: Comparison of auroral ionospheric and field-aligned currents derived from Swarm and ground magnetic field measurements, *J. Geophys. Res. Space Physics*, 121, 9256–9283, <https://doi.org/https://doi.org/10.1002/2016JA022961>, 2016b.
- Juusola, L., Vanhamäki, H., Viljanen, A., and Smirnov, M.: Induced currents due to 3D ground conductivity play a major role in the interpretation of geomagnetic variations, *Ann. Geophys.*, 38, 983–998, <https://doi.org/https://doi.org/10.5194/angeo-38-983-2020>, 2020.
- Juusola, L., Viljanen, A., Dimmock, A. P., Kellinsalmi, M., Schillings, A., and Weygand, J. M.: Drivers of rapid geomagnetic variations at high latitudes, *Ann. Geophys.*, 41, 13–37, <https://doi.org/https://doi.org/10.5194/angeo-41-13-2023>, 2023a.
- Juusola, L., Viljanen, A., Partamies, N., Vanhamäki, H., Kellinsalmi, M., and Walker, S.: Three principal components describe the spatiotemporal development of mesoscale ionospheric equivalent currents around substorm onsets, *Ann. Geophys.*, 41, 483–510, <https://doi.org/https://doi.org/10.5194/angeo-41-483-2023>, 2023b.
- Juusola, L., Vanhamäki, H., Marshalko, E., Kruglyakov, M., and Viljanen, A.: Estimation of the 3-D geoelectric field at the Earth’s surface using Spherical Elementary Current Systems, *EGUsphere*, [preprint], <https://doi.org/https://doi.org/10.5194/egusphere-2024-2831>, 2024.



- 595 Juusola, L., Björnsson, G., Johnsen, M. G., Kauristie, K., Kellinsalmi, M., Matzka, J., Neska, A., Raita, T., Reda, J., Tanskanen, E., Viljanen, A., Willer, A. N., Wittke, J., and Yamauchi, M.: International Monitor for Auroral Geomagnetic Effects (IMAGE) [data set], <https://space.fmi.fi/image>, last access: May 27, 2025, 2025.
- Kamide, Y., Richmond, A. D., and Matsushita, S.: Estimation of ionospheric electric fields, ionospheric currents, and field-aligned currents from ground magnetic records, *J. Geophys. Res.*, 86(A2), 801–813, <https://doi.org/10.1029/JA086iA02p00801>, 1981.
- 600 Karlsson, T., Andersson, L., Gillies, D. M., Lynch, K., Marghitu, O., Partamies, N., Sivadas, N., and Wu, J.: Quiet, Discrete Auroral Arcs — Observations, *Space Sci. Rev.*, 216, <https://doi.org/https://doi.org/10.1007/s11214-020-0641-7>, 2020.
- Kauristie, K.: Magnetometers - Ionospheric Radars - All-sky Cameras Large Experiment (MIRACLE) All-Sky Cameras [data set], <https://space.fmi.fi/MIRACLE/ASC/>, last access: May 27, 2025, 2025.
- Laundal, K. M.: Python interface for the Average Magnetic field and Polar current System (AMPS) model [code], <https://github.com/klaundal/pyAMPS>, last access: May 27, 2025, 2024.
- 605 Laundal, K. M., Finlay, C. C., Olsen, N., and Reistad, J. P.: Solar wind and seasonal influence on ionospheric currents from Swarm and CHAMP measurements, *Journal of Geophysical Research: Space Physics*, 123, 4402–4429, <https://doi.org/https://doi.org/10.1029/2018JA025387>, 2018.
- Laundal, K. M., Yee, J. H., Merkin, V. G., Gjerloev, J. W., Vanhamäki, H., Reistad, J. P., Madelaire, M., Sorathia, K., and Espy, P. J.: Electrojet estimates from mesospheric magnetic field measurements, *Journal of Geophysical Research: Space Physics*, 126, e2020JA028644, <https://doi.org/https://doi.org/10.1029/2020JA028644>, 2021.
- 610 Laundal, K. M., Reistad, J. P., Hatch, S. M., Madelaire, M., Walker, S., Hovland, A. Ø., Ohma, A., Merkin, V. G., and Sorathia, K. A.: Local mapping of polar ionospheric electrodynamics, *Journal of Geophysical Research: Space Physics*, 127, e2022JA030356, <https://doi.org/https://doi.org/10.1029/2022JA030356>, 2022a.
- 615 Laundal, K. M., van der Meeren, C., Burrell, A. G., Starr, G., Reimer, A., Morschhauser, A., and Lamarche, L.: Python wrapper for the Apex fortran library by Emmert et al. [2010] [code], <https://github.com/aburrell/apexpy>, last access: May 27, 2025, 2022b.
- Lehtinen, M. S. and Huuskonen, A.: General incoherent scatter analysis and GUISDAP, *Journal of Atmospheric and Terrestrial Physics*, 58, 435–452, [https://doi.org/https://doi.org/10.1016/0021-9169\(95\)00047-X](https://doi.org/https://doi.org/10.1016/0021-9169(95)00047-X), 1996.
- Machol, J. L., Green, J. C., Redmon, R. J., Viereck, R. A., and Newell, P. T.: Evaluation of OVATION Prime as a forecast model for visible aurorae, *Space Weather*, 10, S03005, <https://doi.org/https://doi.org/10.1029/2011SW000746>, 2012.
- 620 Madelaire, M., Laundal, K., Hatch, S., Vanhamäki, H., Reistad, J., Ohma, A., Merkin, V., and Lin, D.: Estimating the ionospheric induction electric field using ground magnetometers, *Geophysical Research Letters*, 51, e2023GL105443, <https://doi.org/https://doi.org/10.1029/2023GL105443>, 2024.
- Madrigal: Madrigal Database at EISCAT [data set], <https://madrigal.eiscat.se/madrigal/>, last access: May 27, 2025, 2025.
- 625 Marsal, S., Torta, J. M., Segarra, A., and Araki, T.: Use of spherical elementary currents to map the polar current systems associated with the geomagnetic sudden commencements on 2013 and 2015 St. Patrick’s Day storms, *J. Geophys. Res. Space Physics*, 122, 194–211, <https://doi.org/https://doi.org/10.1002/2016JA023166>, 2017.
- Marsal, S., Torta, J. M., Pavón-Carrasco, F. J., Blake, S. P., and Piersanti, M.: Including the temporal dimension in the SECS technique, *Space Weather*, 18, e2020SW002491, <https://doi.org/https://doi.org/10.1029/2020SW002491>, 2020.
- 630 McLay, S. A. and Beggan, C. D.: Interpolation of externally-caused magnetic fields over large sparse arrays using Spherical Elementary Current Systems, *Ann. Geophys.*, 28, 1795–1805, <https://doi.org/https://doi.org/10.5194/angeo-28-1795-2010>, 2010.



- Moen, J. and Brekke, A.: The solar flux influence on quiet time conductances in the auroral ionosphere, *Geophysical Research Letters*, 20, 971–974, <https://doi.org/10.1029/92GL02109>, 1993.
- Newell, P. T., Meng, C.-I., and Lyons, K.: Suppression of discrete aurorae by sunlight, *Nature*, pp. 766–767, <https://doi.org/10.1038/381766a0>, 1996.
- Newell, P. T., Meng, C.-I., and Wing, S.: Relation to solar activity of intense aurorae in sunlight and darkness, *Nature*, 393, 342–344, <https://doi.org/10.1038/30682>, 1998.
- Newell, P. T., Sotirelis, T., and Wing, S.: Diffuse, monoenergetic, and broadband aurora: The global precipitation budget, *J. Geophys. Res.*, 114, A09207, <https://doi.org/10.1029/2009JA014326>, 2009.
- NRC, N. R. C. C.: Penticton Solar Radio Flux at 10.7 cm [data set], [https://lasp.colorado.edu/lisird/data/penticton\\_radio\\_flux](https://lasp.colorado.edu/lisird/data/penticton_radio_flux), last access: May 27, 2025, 2025.
- Palmroth, M., Grandin, M., Sarris, T., Doornbos, E., Tourgaidis, S., Aikio, A., Buchert, S., Clilverd, M. A., Dandouras, I., Heelis, R., Hoffmann, A., Ivchenko, N., Kervalishvili, G., Knudsen, D. J., Kotova, A., Liu, H.-L., Malaspina, D. M., March, G., Marchaudon, A., Marghitsu, O., Matsuo, T., Miloch, W. J., Moretto-Jørgensen, T., Mpouloukidis, D., Olsen, N., Papadakis, K., Pfaff, R., Pirnaris, P., Siemes, C., Stolle, C., Suni, J., van den IJssel, J., Verronen, P. T., Visser, P., and Yamauchi, M.: Lower-thermosphere–ionosphere (LTI) quantities: current status of measuring techniques and models, *Ann. Geophys.*, 39, 189–237, <https://doi.org/10.5194/angeo-39-189-2021>, 2021.
- Papitashvili, N. E. and King, J. H.: OMNI 1-min Data, NASA Space Physics Data Facility, <https://doi.org/10.48322/45bb-8792>, accessed on 28 Apr 2025, 2020.
- Partamies, N., Whiter, D., Kauristie, K., and Massetti, S.: Magnetic local time (MLT) dependence of auroral peak emission height and morphology, *Ann. Geophys.*, 40, 605–618, <https://doi.org/10.5194/angeo-40-605-2022>, 2022.
- Picone, J. M., Hedin, A. E., Drob, D. P., and Aikin, A. C.: NRLMSISE-00 empirical model of the atmosphere: Statistical comparisons and scientific issues, *J. Geophys. Res.*, 107(A12), 1468, <https://doi.org/10.1029/2002JA009430>, 2002.
- Pirjola, R. and Viljanen, A.: Complex image method for calculating electric and magnetic fields produced by an auroral electrojet of finite length, *Ann. Geophys.*, 16, 1434–1444, <https://doi.org/10.1007/s00585-998-1434-6>, 1998.
- Pulkkinen, A., Amm, O., Viljanen, A., and BEAR Working Group: Ionospheric equivalent current distributions determined with the method of spherical elementary current systems, *J. Geophys. Res.*, 108(A2), <https://doi.org/10.1029/2001JA005085>, 2003a.
- Pulkkinen, A., Amm, O., Viljanen, A., and BEAR Working Group: Separation of the geomagnetic variation field on the ground into external and internal parts using the spherical elementary current system method, *Earth, Planets and Space*, 55, 117–129, <https://doi.org/10.1186/BF03351739>, 2003b.
- Richmond, A. D.: Assimilative mapping of ionospheric electrodynamics, *Advances in Space Research*, 12, 59–68, [https://doi.org/10.1016/0273-1177\(92\)90040-5](https://doi.org/10.1016/0273-1177(92)90040-5), 1992.
- Richmond, A. D.: Ionospheric electrodynamics using Magnetic Apex Coordinates, *Journal of geomagnetism and geoelectricity*, 47(2), 191–212, <https://doi.org/10.5636/jgg.47.191>, 1995.
- Richmond, A. D. and Kamide, Y.: Mapping electrodynamic features of the high-latitude ionosphere from localized observations: Technique, *J. Geophys. Res.*, 93(A6), 5741–5759, <https://doi.org/10.1029/JA093iA06p05741>, 1988.
- Ritter, P., Lühr, H., Viljanen, A., Amm, O., Pulkkinen, A., and Sillanpää, I.: Ionospheric currents estimated simultaneously from CHAMP satellite and IMAGE ground-based magnetic field measurements: a statistical study at auroral latitudes, *Ann. Geophys.*, 22, 417–430, <https://doi.org/10.5194/angeo-22-417-2004>, 2004.



- 670 Ritter, P., Lühr, H., and Rauberg, J.: Determining field-aligned currents with the Swarm constellation mission, *Earth, Planets and Space*, 65, 1285–1294, <https://doi.org/https://doi.org/10.5047/eps.2013.09.006>, 2013.
- Robinson, R. M., Kaeppler, S. R., Zanetti, L., Anderson, B., Vines, S. K., Korth, H., and Fitzmaurice, A.: Statistical relations between auroral electrical conductances and field-aligned currents at high latitudes, *Journal of Geophysical Research: Space Physics*, 125, e2020JA028008, <https://doi.org/https://doi.org/10.1029/2020JA028008>, 2020.
- 675 Schunk, R. and Nagy, A.: *Ionospheres: physics, plasma physics, and chemistry*, chap. 4, pp. 72–110, Cambridge University Press, Cambridge, <https://doi.org/https://doi.org/10.1017/CBO9780511635342>, 2009.
- Smith, A. R. A., Paões, M., and Santillan, D.: *ESA-VirES/VirES-Python-Client* [code], <https://doi.org/10.5281/zenodo.2554162>, last access: May 27, 2025, 2025.
- Stafford, B.: *Pysolar* [code], <https://github.com/pingswept/pysolar>, last access: May 27, 2025, 2014.
- 680 van de Kamp, M.: Harmonic quiet-day curves as magnetometer baselines for ionospheric current analyses, *Geosci. Instrum. Method. Data Syst.*, 2, 289–304, <https://doi.org/https://doi.org/10.5194/gi-2-289-2013>, 2013.
- Vanhamäki, H. and Juusola, L.: Introduction to Spherical Elementary Current Systems, in: *Ionospheric Multi-Spacecraft Analysis Tools*, pp. 5–33, ISSI Scientific Report Series 17, <https://doi.org/https://doi.org/10.1007/978-3-030-26732-2>, 2020.
- Vanhamäki, H., Amm, O., and Viljanen, A.: Role of inductive electric fields and currents in dynamical ionospheric situations, *Ann. Geophys.*, 25, 437–455, <https://doi.org/https://doi.org/10.5194/angeo-25-437-2007>, 2007.
- 685 VirES: VirES for Swarm [server], <https://vires.services>, last access: May 27, 2025, 2025.
- Walker, S., Laundal, K., Reistad, J., Ohma, A., and Hatch, S.: Statistical temporal variations in the auroral electrojet estimated with ground magnetometers in Fennoscandia, *Space Weather*, 21, e2022SW003305, <https://doi.org/https://doi.org/10.1029/2022SW003305>, 2023.
- Wang, Z. and Zou, S.: COMPASS: A new CONductance Model based on PFISR And SWARM Satellite observations, *Space Weather*, 20, e2021SW002958, <https://doi.org/https://doi.org/10.1029/2021SW002958>, 2022.
- 690 Weygand, J. M. and Wing, S.: Comparison of DMSP and SECS region-1 and region-2 ionospheric current boundary, *Journal of Atmospheric and Solar-Terrestrial Physics*, 143–144, 8–13, <https://doi.org/https://doi.org/10.1016/j.jastp.2016.03.002>, 2016.
- Weygand, J. M., Amm, O., Viljanen, A., Angelopoulos, V., Murr, D., Engebretson, M. J., Gleisner, H., and Mann, I.: Application and validation of the spherical elementary currents systems technique for deriving ionospheric equivalent currents with the North American and Greenland ground magnetometer arrays, *J. Geophys. Res.*, 116, <https://doi.org/https://doi.org/10.1029/2010JA016177>, 2011.
- 695 Yee, J.-H., Gjerloev, J., Perez, R., Swartz, W. H., Misra, S., Chidambaram, O., and Ruf, C.: The EZIE way to measure the ionospheric electrojets with a three-cubesat constellation, in: *Proceedings of the Small Satellite Conference, Technical Session 6: Science/Mission Payloads*, SSC21-VI-07, <https://digitalcommons.usu.edu/smallsat/2021/all2021/177/>, 2021a.
- Yee, J.-H., Gjerloev, J., and Wu, D.: Remote sensing of magnetic fields induced by electrojets from space, in: *Upper Atmosphere Dynamics and Energetics*, American Geophysical Union, <https://doi.org/https://doi.org/10.1002/9781119815631.ch21>, 2021b.
- 700 Yoshikawa, A., Nakamizo, A., Amm, O., Vanhamäki, H., Fujii, R., Tanaka, Y.-M., Uozumi, T., Yumoto, K., and Ohtani, S.: Self-consistent formulation for the evolution of ionospheric conductances at the ionospheric E region within the M-I coupling scheme, *J. Geophys. Res.*, 116, <https://doi.org/10.1029/2011JA016449>, 2011.
- Zhang, Y., Paxton, L. J., Schaefer, R., and Swartz, W. H.: Thermospheric conditions associated with the loss of 40 Starlink satellites, *Space Weather*, 20, e2022SW003168, <https://doi.org/https://doi.org/10.1029/2022SW003168>, 2022.
- 705

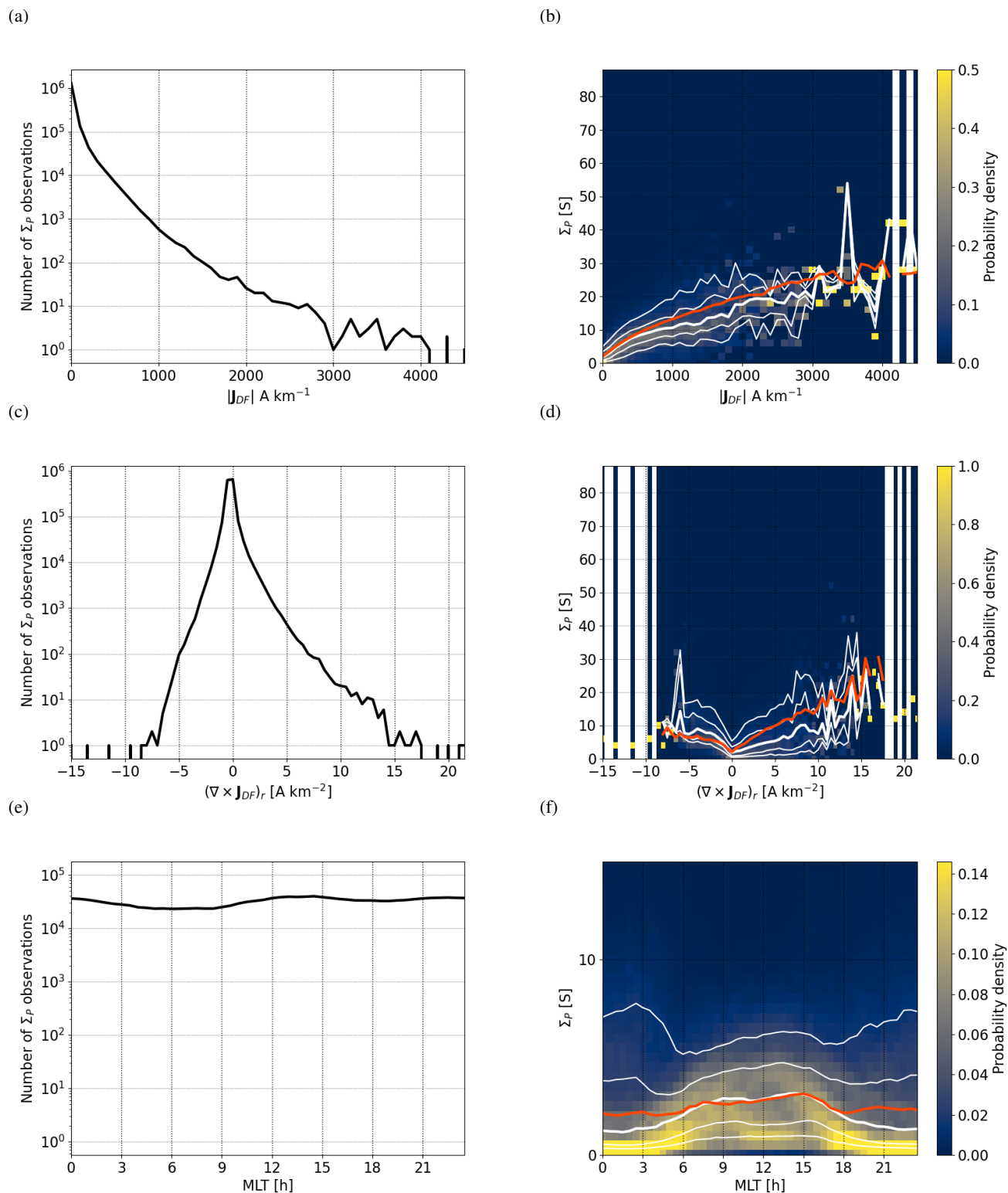


**Figure 3.**  $\Sigma_P$  as a function of  $|J_{DF}|$ ,  $(\nabla \times J_{DF})_r$ , and MLT in a format similar to Fig. 1. Whenever there is no conductance data for a given value on the x-axis, the corresponding distribution is replaced by a white bar.

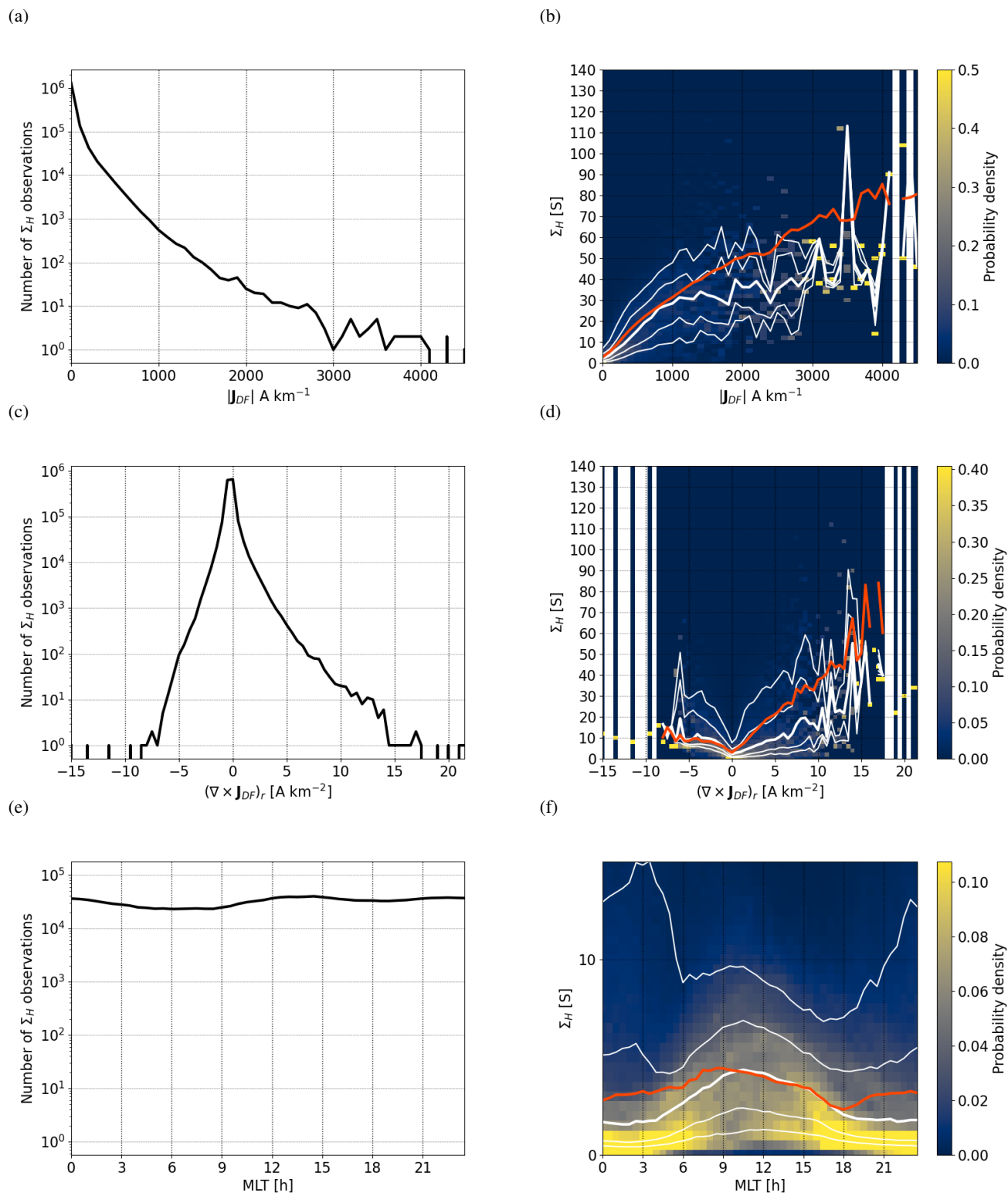


**Figure 4.** The same as Figure 3 except for the Hall conductance  $\Sigma_H$  instead of the Pedersen conductance  $\Sigma_P$ .

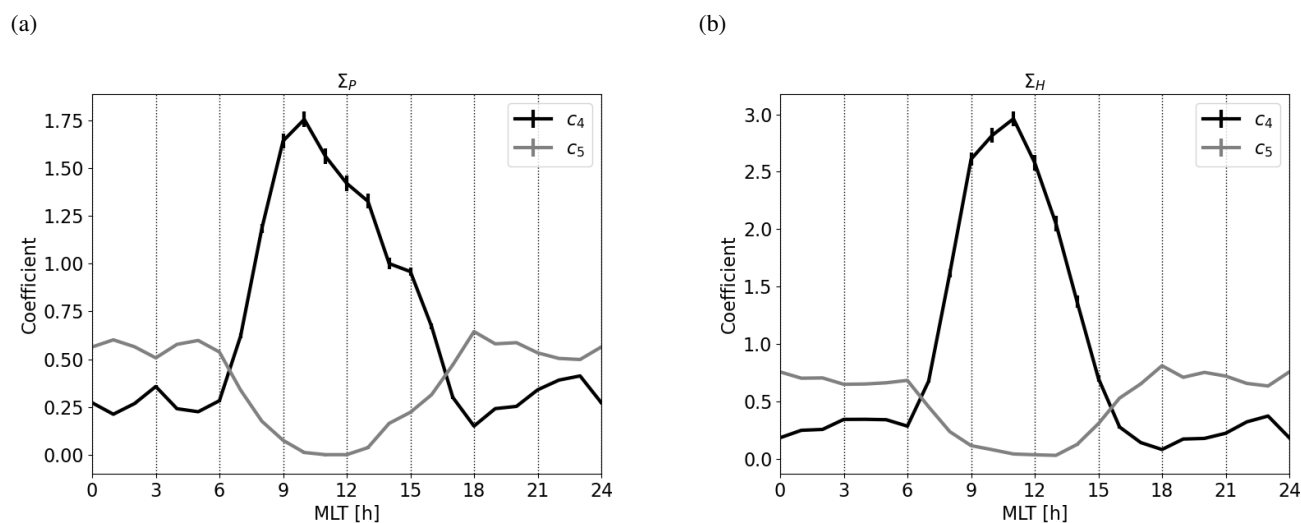


**Figure 5.** Coefficients  $c_4$  and  $c_5$  from Eq. 33 as a function of MLT for  $\Sigma_P$  (a) and  $\Sigma_H$  (b). Standard deviation errors of the coefficients are indicated by vertical line segments.

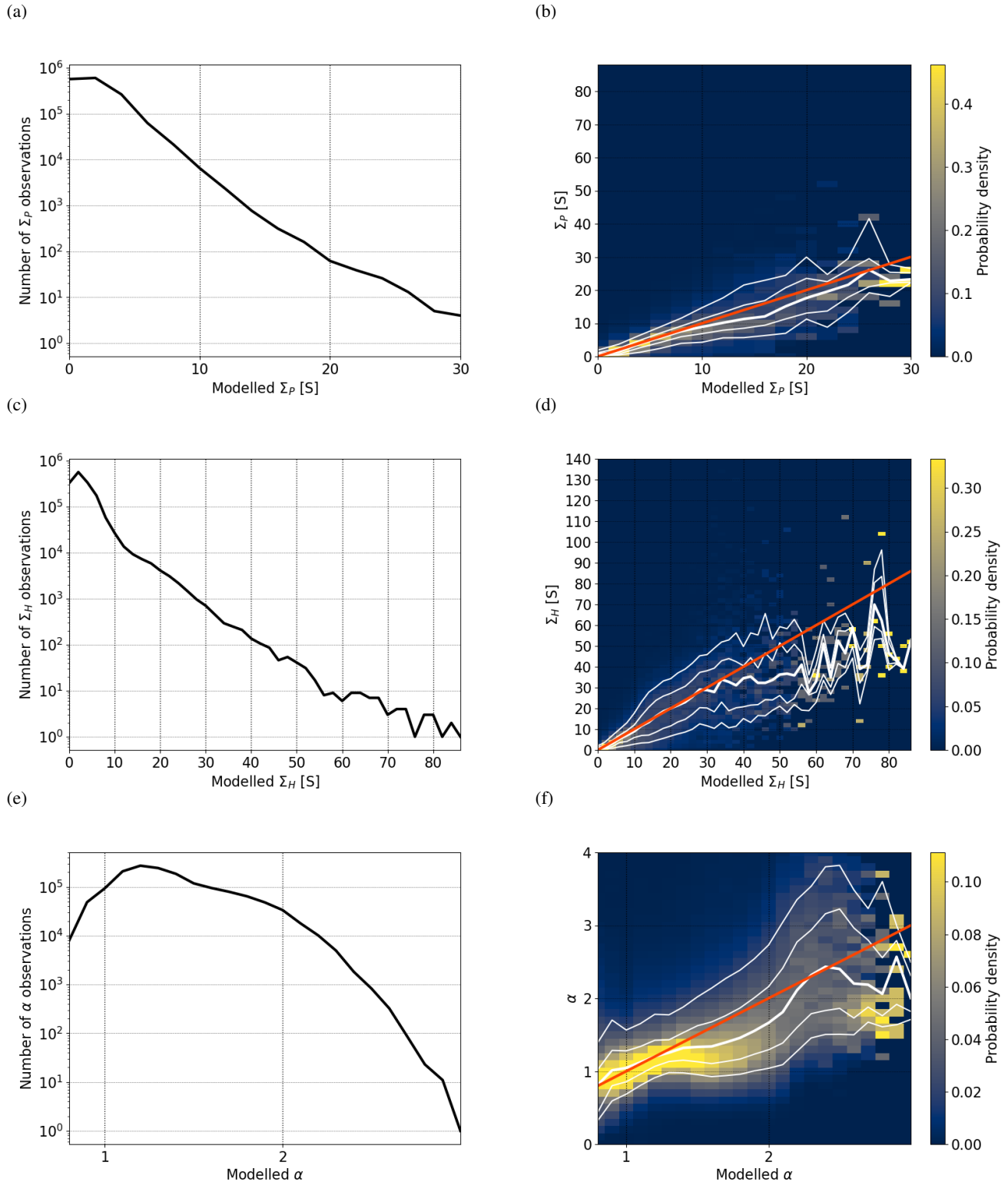


**Figure 6.** Observed  $\Sigma_P$  (top),  $\Sigma_H$  (middle), and Hall-to-Pedersen conductance ratio  $\alpha = \frac{\Sigma_H}{\Sigma_P}$  (bottom) as a function of the modelled value in a format similar to Fig. 1–4. The red line is the line of unity.

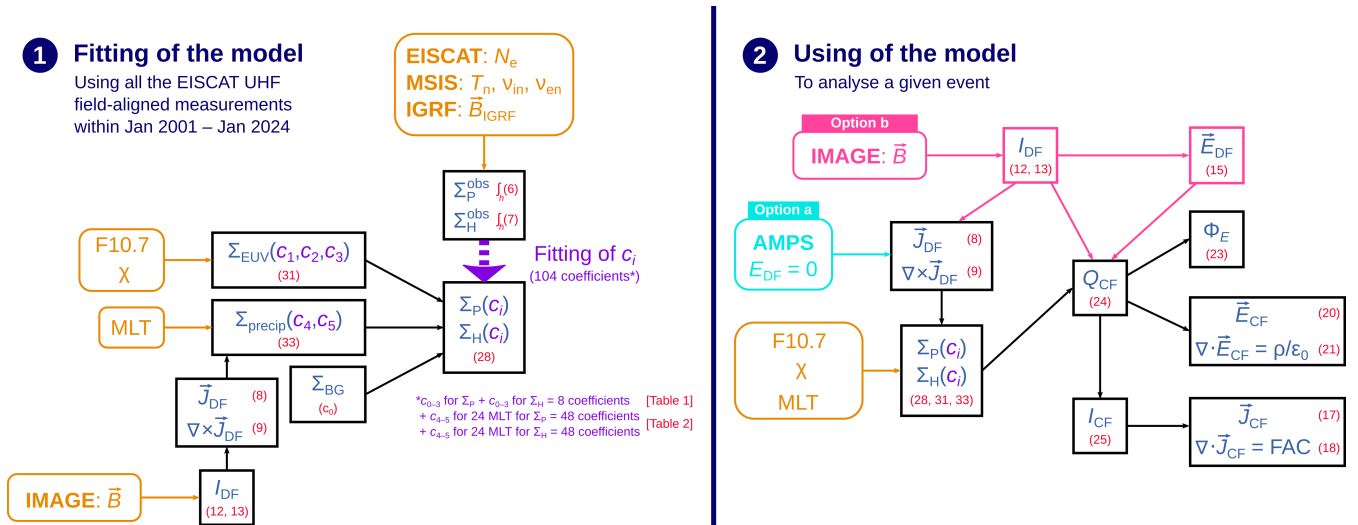


**Figure 7.** Summary of fitting of the model (1) and of using the model (2). Input data are in yellow, derived parameters in blue, model coefficients in purple, and equation numbers in red. The right hand side illustrates how the model is used in section 3.2 (“Option a”, cyan color) and section 3.3 (“Option b”, pink color).

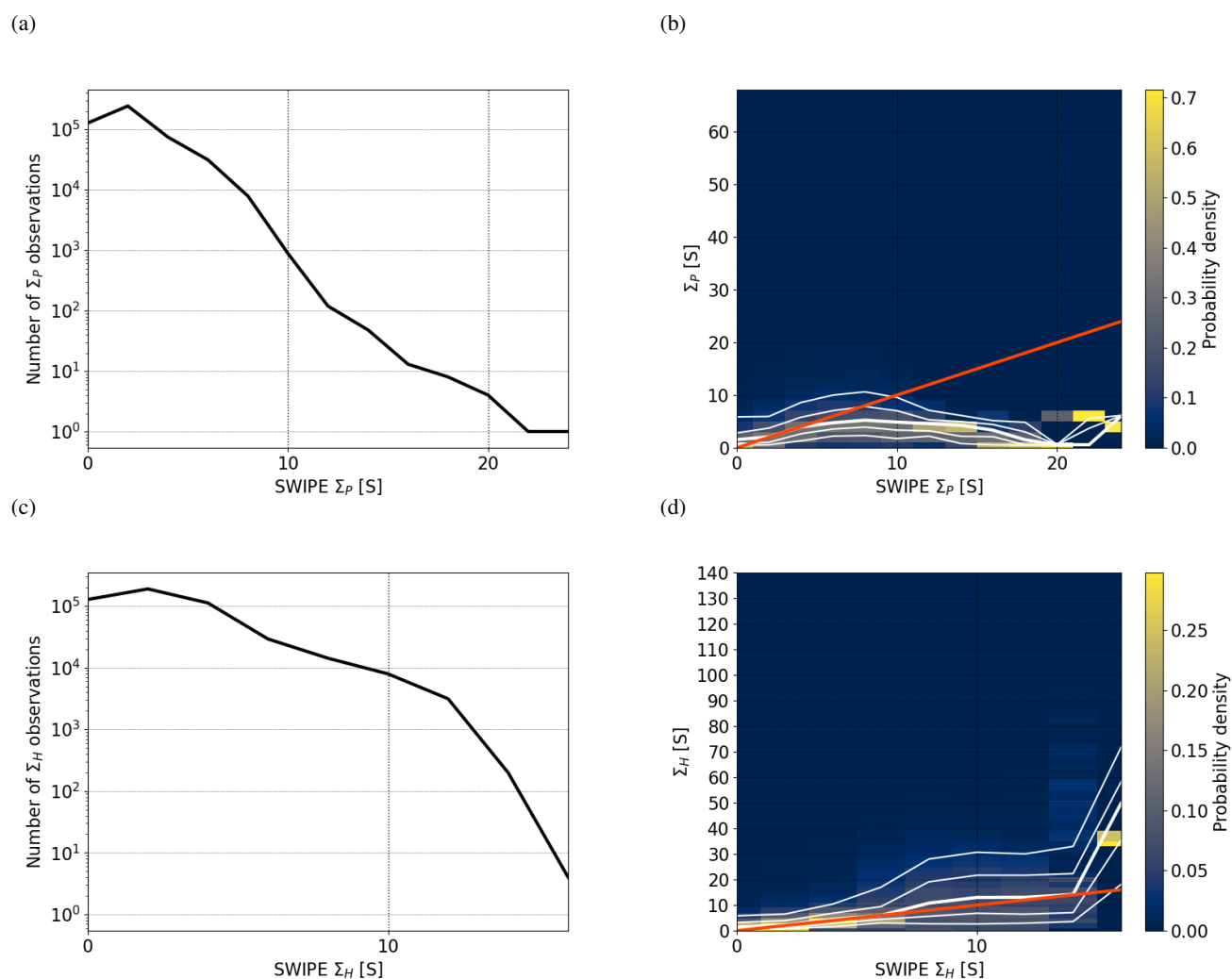
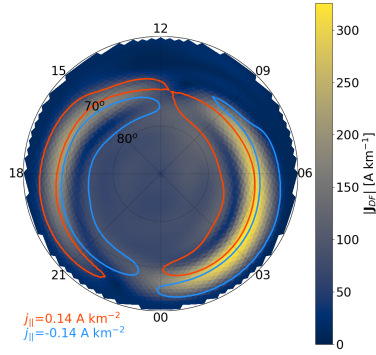


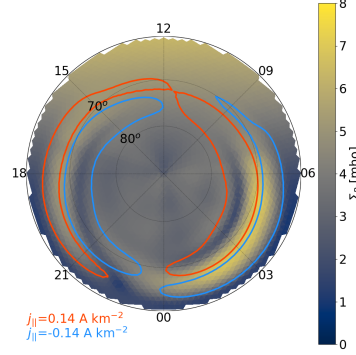
**Figure 8.** The same as Fig. 6a–d except that instead of the new EISCAT-based model, values modelled using SWIPE are compared with the EISCAT observations. 



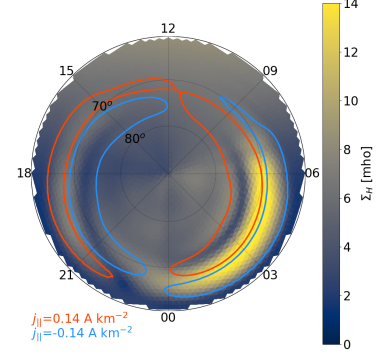
(a) AMPS  $|\mathbf{J}_{DF}|$



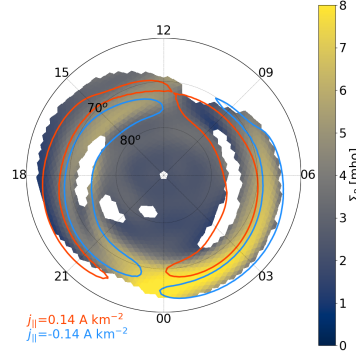
(b) AMPS-EISCAT  $\Sigma_P$



(c) AMPS-EISCAT  $\Sigma_H$



(d) SWIPE  $\Sigma_P$



(e) SWIPE  $\Sigma_H$

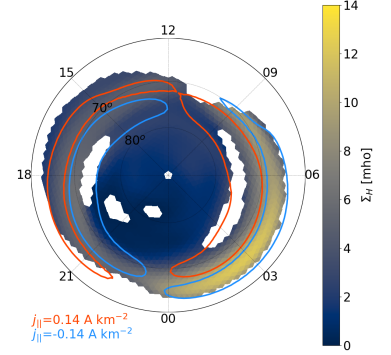
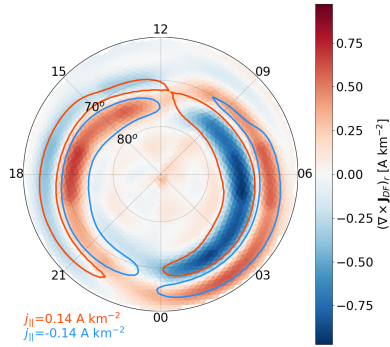


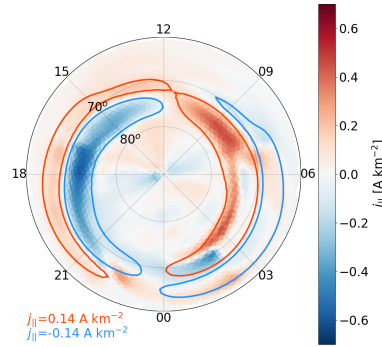
**Figure 9.** (a):  $|\mathbf{J}_{DF}|$  as a function of magnetic latitude and MLT according to the AMPS model (Laundal et al., 2018) for dipole tilt angle  $0^\circ$  (equinox), solar wind speed  $V = 450$  km/s,  $F_{10.7} = 120$  sfu, IMF  $B_{GSM,y} = 0$  nT and  $B_{GSM,z} = -5$  nT. The contours indicate regions of upward (blue) and downward (red) field-aligned current density according to AMPS. (b):  $\Sigma_P$  according to the EISCAT-based empirical model for the AMPS  $\mathbf{J}_{DF}$ . (c):  $\Sigma_H$  according to the EISCAT-based empirical model for the AMPS  $\mathbf{J}_{DF}$ . (d):  $\Sigma_P$  according to the SWIPE model (Hatch et al., 2024) for the same conditions as AMPS. (e):  $\Sigma_H$  according to the SWIPE model. The red and blue contours are the same in all panels.



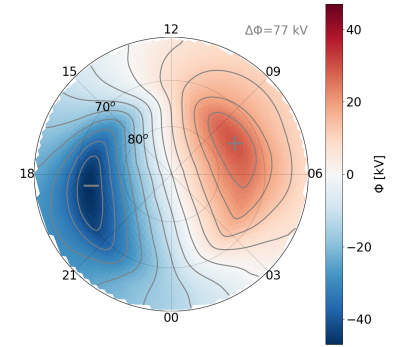
(a) AMPS  $(\nabla \times \mathbf{J})_r$



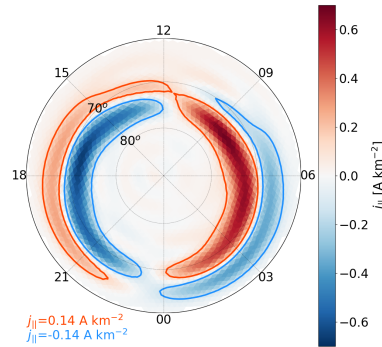
(b) AMPS-EISCAT field-aligned current density



(c) AMPS-EISCAT electric potential



(d) AMPS field-aligned current density



(e) SWIPE electric potential

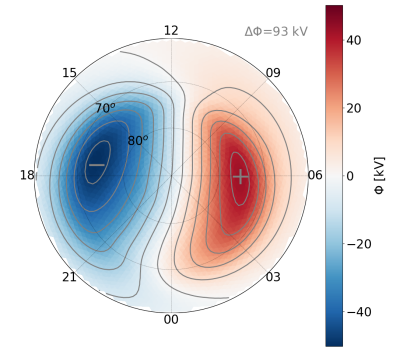


**Figure 10.** (a):  $(\nabla \times \mathbf{J})_r$  as a function of magnetic latitude and MLT according to the AMPS model (Laundal et al., 2018) for the same model parameters as Fig. 9. (b–c): Field-aligned current density and electric potential solved using Eq. 24 and Eq. 25 and the distributions in Fig. 9a, 9b, 9c, and 10a.  $E_{DF}$  is assumed to be negligible. (d): Field-aligned current density according to the AMPS model. The contours indicate regions of upward (blue) and downward (red) field-aligned current density with amplitude exceeding  $0.14 \text{ A/km}^2$ . (e): Electric potential according to the SWIPE model (Hatch et al., 2024). The red and blue contours in (a) and (b) are identical to those in panel (d).

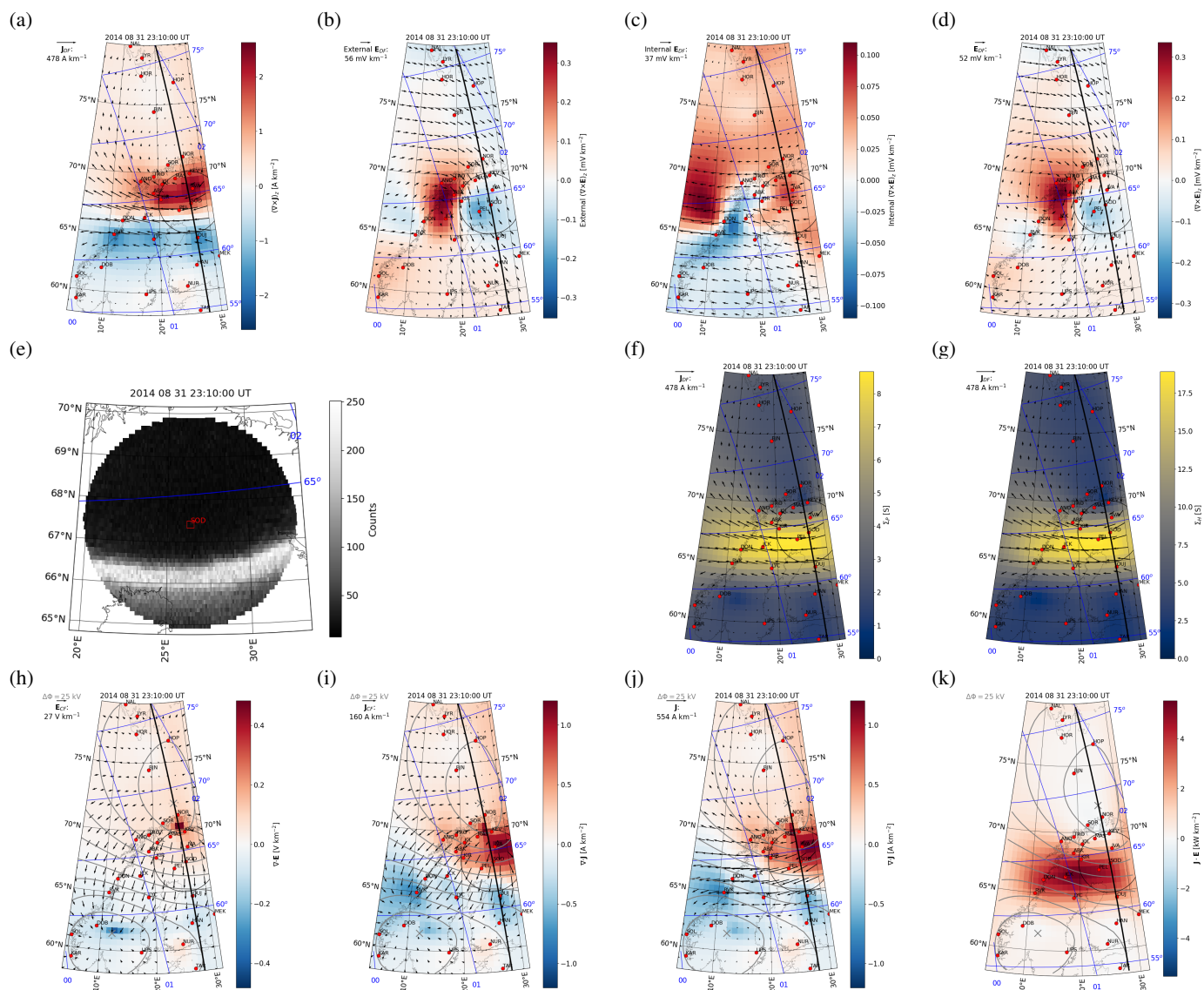




**Figure 11.** Morning sector auroral arc event on 31 August 2014 at 23:10:00 UT. (a): Divergence-free part of the ionospheric horizontal current density (external  $\mathbf{J}_{DF}$ , arrows) and its curl ( $(\nabla \times \mathbf{J}_{DF})_z = -(\nabla \times \mathbf{J}_{DF})_r$ , color) as a function of geographic latitude and longitude, derived from IMAGE magnetometer data. Locations of the IMAGE stations used in the analysis are indicated by the red circles, apex coordinates (Richmond, 1995; Emmert et al., 2010; Laundal et al., 2022b) with the blue grid, the SOD all-sky camera field-of-view by the black circle, and the track of the Swarm A satellite by the black line. (b–d): External part, internal part, and total ionospheric divergence-free electric field ( $\mathbf{E}_{DF}$ , arrows) and its curl ( $(\nabla \times \mathbf{E}_{DF})_z$ , color). (e): Auroral intensity from the SOD all-sky camera mapped to 110 km altitude. (f–g): Pedersen conductance ( $\Sigma_P$ , color) and Hall conductance ( $\Sigma_H$ , color) according to the EISCAT-based empirical model for  $\mathbf{J}_{DF}$  (arrows). (h): Curl-free horizontal ionospheric electric field ( $\mathbf{E}_{CF}$ , arrows) and its divergence ( $\nabla \cdot \mathbf{E}_{CF}$ , color). (i): Curl-free horizontal ionospheric current density ( $\mathbf{J}_{CF}$ , arrows) and its divergence ( $\nabla \cdot \mathbf{J}_{CF} = j_z = -j_r$ , color). (j): Total horizontal ionospheric current density ( $\mathbf{J} = \mathbf{J}_{DF} + \mathbf{J}_{CF}$ , arrows) and its divergence ( $\nabla \cdot \mathbf{J} = j_z = -j_r$ , color). (k): Dot product between the total horizontal current density and electric field ( $\mathbf{J} \cdot \mathbf{E}$ ). The gray contours show the electric potential  $\Phi$ . The maximum potential difference  $\Delta\Phi$  between the locations indicated by the gray crosses is given in the top left corner.

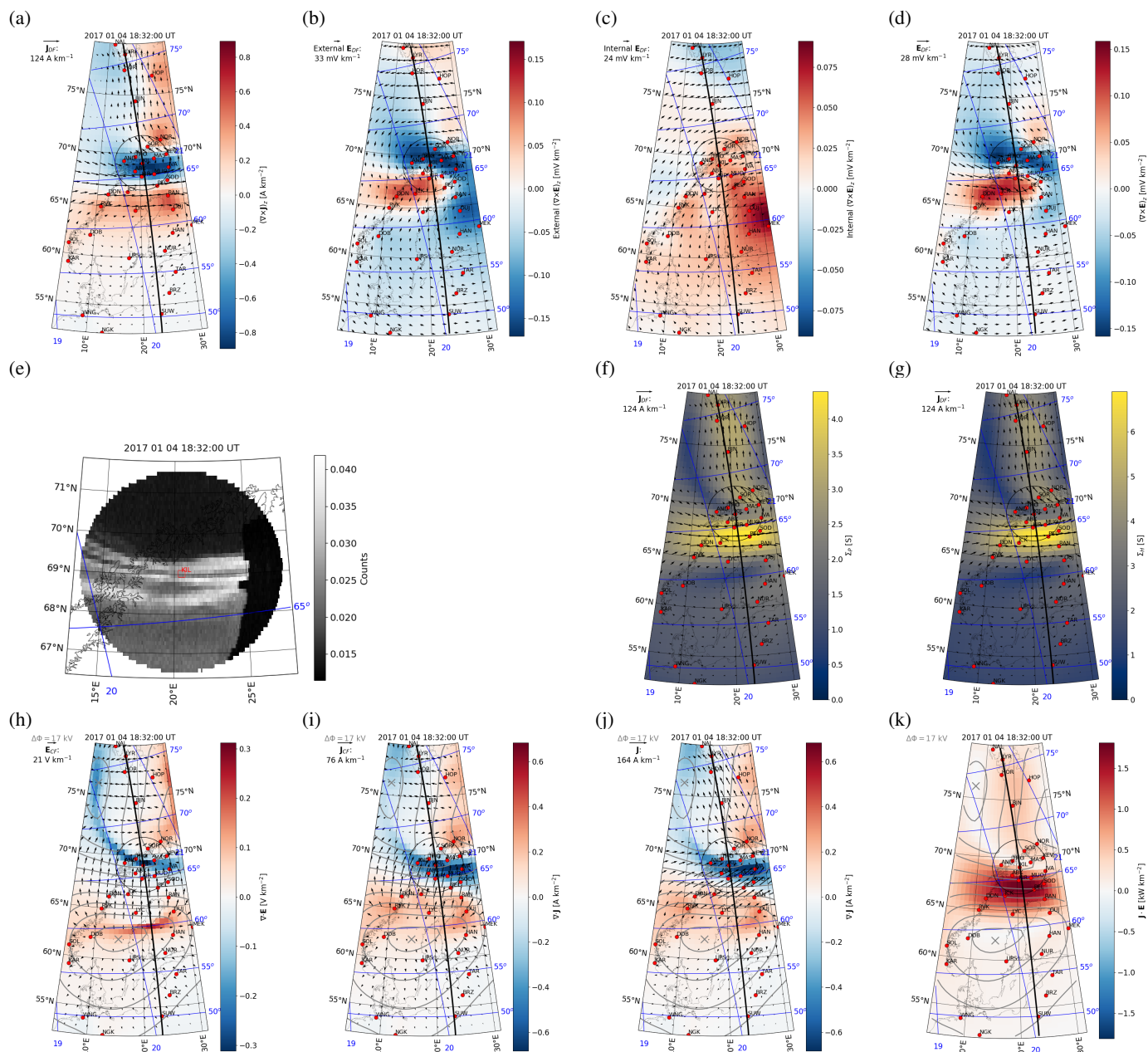
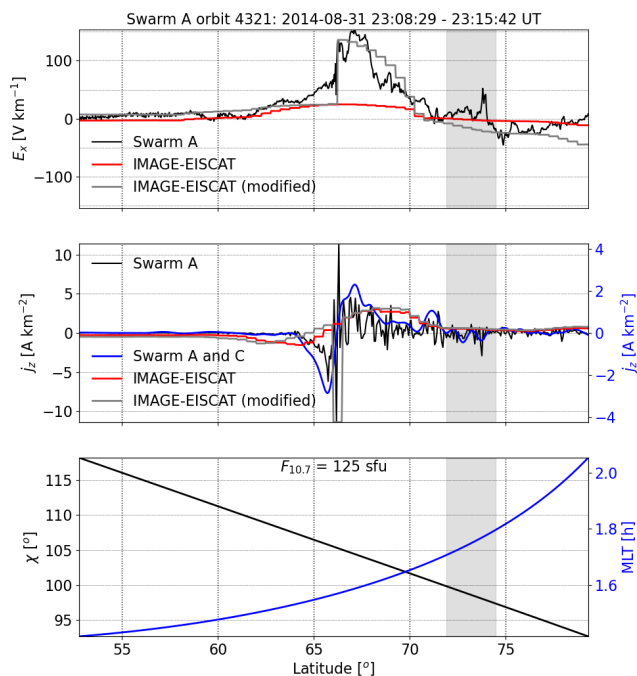


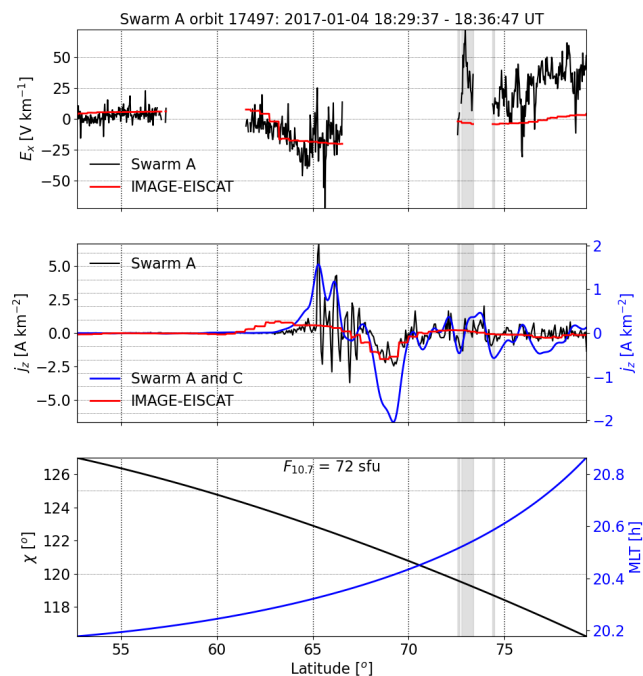
**Figure 12.** An evening sector auroral arc event on 4 January 2017 at 18:32:00 UT in the same format as Fig. 11. The all-sky camera is KIL instead of SOD.



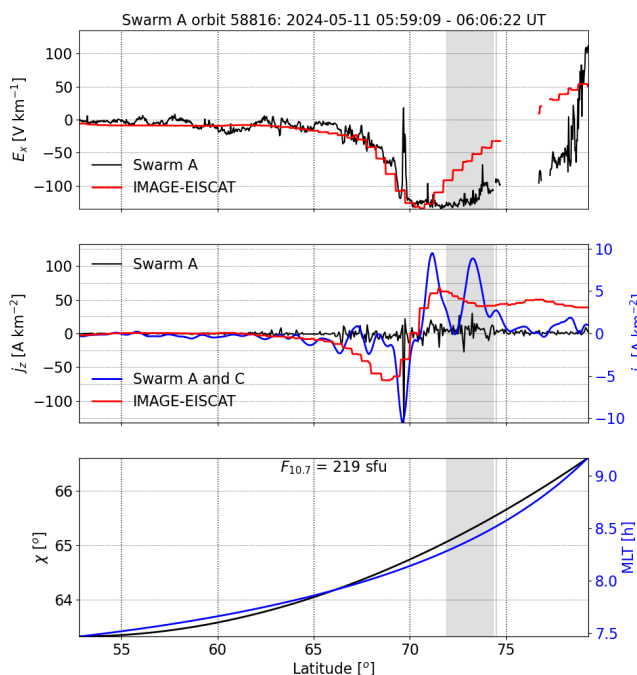
(a)



(b)



(c)



(d)

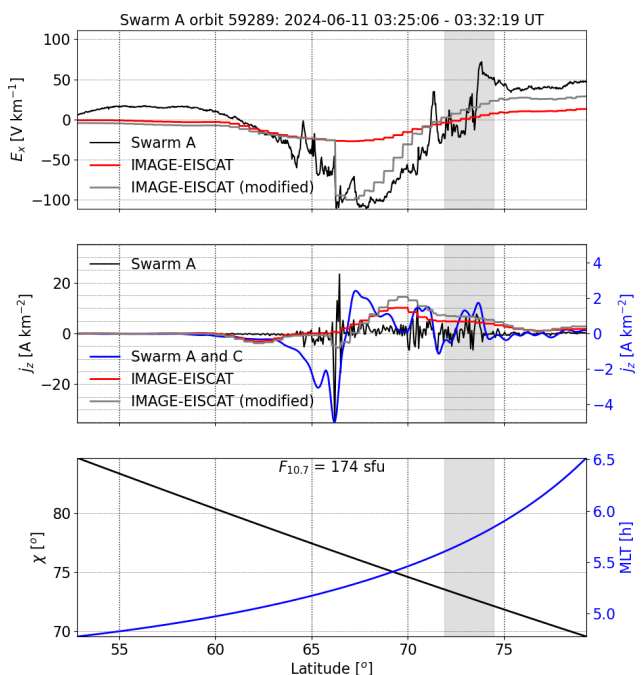




**Figure 13.** Four Swarm crossings of IMAGE (a–d). Top: Ionospheric electric field component corresponding to the ion drift measured by Swarm A perpendicular to the satellite orbit (black) and IMAGE-EISCAT estimate of the same component (red). Middle: Radial current density estimated from Swarm A using the single satellite method (Ritter et al., 2013) (black, left scale), from the Swarm A and C satellite pair using the dual-satellite method (Ritter et al., 2013) (blue, right scale), and the EISCAT-IMAGE estimate (red, right scale). Bottom: Sun zenith angle  $\chi$  (black; left scale) and MLT (blue; right scale). The gray curves in the top and middle panels of crossings (a) and (d) are otherwise the same as the red curves except that a modified conductance model (Section 4.2) is used.

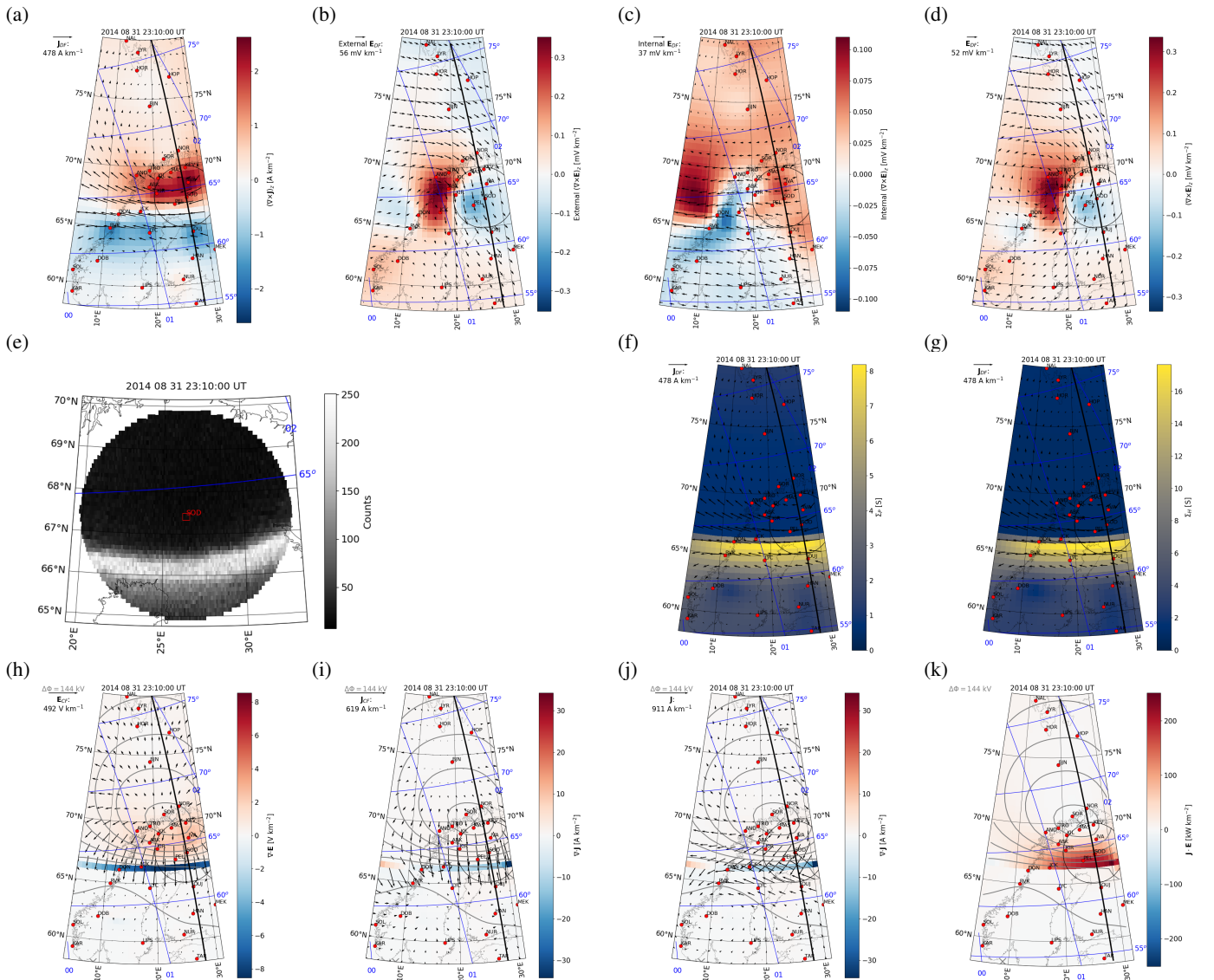


**Figure 14.** The same as Fig. 11 except that the conductance model has been modified as described in Section 4.2. Panels a–f are identical to those in Fig. 11, but they are repeated for easier comparison.